

**Linear Spectroscopic Studies of Semiconductor Quantum  
Wells**

by

**M. W. Day**

A thesis submitted to the  
Faculty of the University of Colorado in partial fulfillment  
of the requirements for Honors' designation for the degree of

Bachelor of Science

Department of Physics

2015

This thesis entitled:  
Linear Spectroscopic Studies of Semiconductor Quantum Wells  
written by M. W. Day  
has been approved for the Department of Physics

---

Prof. Steven Cundiff

---

Prof. James Thompson

---

Prof. Judith Packer

Date \_\_\_\_\_

The final copy of this thesis has been examined by the signatories, and we find that both the content and the form meet acceptable presentation standards of scholarly work in the above mentioned discipline.

Day, M. W. (B.S. )

Linear Spectroscopic Studies of Semiconductor Quantum Wells

Thesis directed by Prof. Steven Cundiff

Manufacturing processes unintentionally introduce fluctuations in the width of semiconductor quantum wells. These fluctuations subtly modulate the optical emission energies of exitons confined within the quantum well layer. It is therefore imperative to quantify these width fluctuations so their effect on exciton confinement potentials can be accounted for in ultrafast spectroscopic studies of semiconductor quantum wells. The use of microphotoluminescence spectroscopy makes quantifying this disorder possible. I present microphotoluminescence spectroscopy work taken in pursuit of an Honors' thesis.

## **Dedication**

Long Dedication

## Acknowledgements

Long Ack

## Contents

### Chapter

<b>1</b>	<b>Introduction</b>	<b>1</b>
<b>2</b>	<b>Theory and Background</b>	<b>4</b>
2.1	The Semiconductor Quantum Well . . . . .	4
2.1.1	Bandgap . . . . .	4
2.1.2	Confinement . . . . .	7
2.1.3	The Exciton . . . . .	11
2.2	Quantum Well Disorder . . . . .	14
2.3	Exciton Coupling in Asymmetric Double Quantum Wells . . . . .	16
2.4	Microphotoluminescence Spectroscopy . . . . .	16
2.5	Photoluminescence Excitation Spectroscopy . . . . .	19
<b>3</b>	<b>Experimental Methods</b>	<b>21</b>
3.1	The Light Source . . . . .	21
3.2	Optical Components and Optical Path Configuration for $\mu$ PL Experiments .	23
3.2.1	Manufacturing the SIL . . . . .	23
3.2.2	Manufacturing the Cryostat Optics Mount . . . . .	25
3.2.3	Experimental Optical Path Configuration . . . . .	26
3.3	$\mu$ PL Data Collection . . . . .	29
3.3.1	Optical Alignment Considerations . . . . .	29

3.3.2	Data Collection Process . . . . .	30
3.4	Optical Components and Optical Path Configuration for PLE Experiments .	31
3.4.1	Optical Path Configuration and Alignment . . . . .	31
3.4.2	Data Collection for Photoluminescence Excitation Spectroscopy . . .	32
<b>4</b>	<b>Disorder in Quantum Well Structures</b>	<b>34</b>
4.1	$\mu$ PL Results and Analysis for Multiple Quantum Well Samples . . . . .	34
4.1.1	Disorder in a Ten Quantum Well Structure . . . . .	34
4.1.2	Disorder in a Four Quantum Well Structure . . . . .	39
4.1.3	Disorder in an Interfacial Quantum Dot Structure . . . . .	41
4.2	PLE Results and Analysis . . . . .	43
<b>5</b>	<b>Conclusion and Future Work</b>	<b>48</b>
5.1	Conclusions from Linear Spectroscopic Experiments . . . . .	48
5.2	Future Work . . . . .	49
<b>Bibliography</b>		<b>50</b>

## Figures

### **Figure**

2.1 A typical dispersion curve minima for a direct-gap semiconductor. An optical transition is illustrated at $k = 0$ , where an electron is absorbing a photon resulting in a transition from the conduction band to the valance band. . . . .	6
2.2 The band structure of GaAs, the allowed states are the thick horizontal curves, and the boxed region is the direct-gap region, in which electrons can be make direct transitions across the bandgap. Note, the minima of this region look like the dispersion curve in figure 2.1 [7]. .	7
2.3 A graphical representation of the one-dimensional infinite potential well of width $L$ .	8
2.4 An example of the semiconductor quantum well. These layers can be repeated arbitrarily many times. .	10
2.5 A simple model for the behavior of an exciton in a quantum well, suitable for the work completed herein. .	13
2.6 An STM picture of the GaAs growth front, stopped mid-growth, of a 110 oriented sample. The shown defect size is roughly representative of disorder in modern GaAs samples grown by molecular beam epitaxy. However, defect size and shape is highly sample dependent, so disorder varies widely from one QW structure to the next. Note, the disorder terraces are on the order of 100nm across. Adapted from [21]. . . . . . . . . . . . . . . . . . .	15

2.7	In a), the energy of a ground state exciton located in a portion of the QW of average thickness, the blue line in b) depicts the ground state energy of an exciton located in a slightly thinner than average portion of the QW, and in c), the blue line depicts the ground state energy of an exciton located in a slightly thicker than average portion of the QW. In both b) and c), the average exciton ground state energy is depicted by the maroon dashed line.	15
2.8	A representation of a confocal optical geometry used to collect the PL from the QW sample. The PL image is being collected from a small region of the QW sample, magnified, and then collimated by the two lenses.	18
2.9	A representation of the principle of our specific $\mu$ PL experiment. The PL image leaves the SIL normal to the hemispheric surface, so it just increases $n$ and lowers the diffraction limit.	19
3.1	A depiction of the modified mount: the actuator arm fits into a sleeve attached by a pivot to the rotating filter mount. A spring attached to both the rotating mount and aluminum block holds the sleeve to the actuator and ensures smooth rotation in either direction.	22
3.2	A depiction of the modified mount: the actuator arm fits into a sleeve attached by a pivot to the rotating filter mount. A spring attached to both the rotating mount and aluminum block holds the sleeve to the actuator and ensures smooth rotation in either direction.	23
3.3	A depiction of the lapp. The orange casing is copper while the grey lining is lead solder. The cavity left by the ball bearing was smooth enough to polish the relatively soft ZnSe hemispheres to an optical quality finish.	24
3.4	A depiction of the polishing setup in the lathe. The off-center placement of the lapp and lapp pin allowed the lapp to rotate and move slightly to randomize the SIL polishing.	25

3.5 A representation of the optics inside the cryostat. The optics were held in place relative to each other by a gold-plated copper mounting tube, containing the lenses. This mounting tube was affixed to a mirror which directed the excitation beam into the cryostat optics and eventually the sample. . . . .	27
3.6 A diagram of the experimental components. The second telescope was an optional feature, its use doubled the system magnification. The light pink beam is the PL signal, while the red beam is the excitation laser. . . . .	28
3.7 A depiction of the PL spot on the spectrometer slit. The spot translates across the slit as we move the lens on the translation stage, allowing us to take vertical slices of the image as it translates across the slit. . . . .	29
3.8 A flowchart depicting the LabView code processing sequence. Each set of $\mu$ PL data was acquired using this process, where $s_s$ was the lens step size and $i_0$ was the number of data collection steps to be run. . . . .	31
3.9 A diagrammatic representation of the PLE experiment. The red beam is the excitation laser while the pink beam is the PL signal. We used a long pass filter (LPF) to cut out any light with wavelength lower than 800nm, as we suspected some of the pump scatter (green) was making it to the sample, reducing our ability to control the excitation wavelength. . . . .	32
3.10 A flowchart depicting the LabView code processing sequence for the PLE experiments. Each set of PLE data was acquired using this process, where $\lambda_{step}$ was the wavelength step size and $i_0$ was the number of data collection steps to be run. . . . .	33
4.1 A raw CCD image corresponding to one vertical slice of the PL image. In order to calculate the PL emission wavelength as a function of sample location, we found the maximum PL amplitude as a function of vertical sample position for each vertical slice. . . . .	35

4.2 A vertical 10QW PL amplitude slice from a CCD raw image. Effectively, these slices were stacked together along the lens translation axis to recover the second sample location axis and build a 3D surface of either PL amplitude or PL energy. . . . .	36
4.3 A reconstructed PL image of 10QW sample surface. The small features in the image correspond to striations and dust on the surface of the sample. The excitation spot's maximum intensity occurred near the bottom of the image, corresponding to the PL amplitude maximum. . . . .	37
4.4 A $\mu$ PL energy deviation image for the 10QW sample. Note the energy deviation was found to be 0.1meV, peak to peak, at maximum. . . . .	38
4.5 A reconstructed image of the PL amplitude of the 4QW sample. . . . .	40
4.6 An energy deviation map for the 4QW sample. . . . .	40
4.7 An energy deviation map for the IQD sample. The energy deviations in the IQD sample are much larger than those measured in the 4QW and 10QW samples, even though the IQD structure is periodic and suffers from similar spectral averaging the other two samples do. . . . .	42
4.8 An example set of PLE data taken on AQW samples. The grey circle corresponds to a coupling peak between wells in the Stokes direction: the narrow well absorbs the laser excitation, while the wide wells emit a portion of the absorbed energy. The red circle corresponds to a coupling peak in the anti-Stokes direction: the wide well absorbs and the narrow well emits a portion of the excitation energy. The diagonal white trace is the laser scatter. . . . .	44
4.9 A set of three PLE vertical profiles taken at the wavelength of peak emission intensity for a) the 30nm, b) the 10nm, and c) the 5nm barrier width AQW. Note: the narrow well emission intensity was much lower than the wide well emission intensity, and was scaled up for graphical comparison. . . . .	45

- 4.10 Temperature dependance for the PLE coupling peaks for barrier width of a)  
30nm, b) 10nm, and c) 5nm. The intensity of coupling between wells seems  
to peak at some low temperature, and then decrease as sample temperature  
increases. . . . . 47

## Chapter 1

### Introduction

Recent advances in nanoscale semiconductor manufacturing techniques allow for the realization of unique nanostructures ideally suited for a broad range of optical and electronic devices. Precise control of material geometry and immense parametric freedom during device fabrication makes tailoring semiconductor nanostructures to their applications relatively easy. With these processes, confining charge carriers on the scale of their de Broglie wavelengths becomes possible. Nanostructures employing confinement on such small scales have proven to be especially useful. A particularly useful subset of these structures, known as quantum wells, confine their charge carriers in just one dimension. It is therefore possible to create such useful devices as highly efficient photo- and laser diodes. Additionally quantum wells (QWs) have shown particular promise in such diverse areas as quantum information processing CITE QI REVIEW, as low noise transistors, and as saturable absorbers in mode-locked lasers. In addition to their applications, QWs have proven useful as a testbed for studying the quantum interactions between light and matter CITE Steve Review.

Despite immense progress in the growth of quantum wells, manufacturing processes still unintentionally introduce inhomogeneities to the layer thickness during crystal deposition. This translates to an uneven interface between two different materials on the scale of a few crystal monolayers. What this means for a quantum well structure is that small fluctuations in interface flatness translate to small fluctuations in well width as these happen at both interfaces of the quantum well and barrier layers. These small width fluctuations are known

as structural disorder.

Disorder affects charge carrier mobility within QWs, which can affect device efficiency and optical activity. Because of the ubiquity of QW structures, it is important to characterize disorder. Being able to quantitatively map structural disorder within QWs can help manufacturers improve the uniformity of their QWs, and in turn the quality and efficiency of their devices. For use of QWs in optical experiments, quantifying the spatial distribution of disorder is important because complete information concerning inhomogeneous contributions to the overall spectral response of QWs can help us enrich our understanding of many-body physics of excitons within quantum wells.

The local thickness of a QW structure can be optically determined: simply by spectrally resolving the total emission signal from a photo-excited QW, allows one to determine the average thickness of a QW layer CITE Gilleo. Structural QW disorder modifies the thickness on the well at nanometer scale and therefore slightly modulates the energies of the emitted photons as a function of position within the QW system. Therefore, disorder can be experimentally quantified. By obtaining a spatial map of QW emission energies with sufficient resolution spatial and spectral resolution, we can determine the local well thickness and therefore obtain a quantitative picture of disorder within a QW. By optically exciting a QW sample and spectrally imaging the emitted light, a linear spectroscopic technique known as micro-photoluminescence spectroscopy, we recover a spatially resolved map of emission energies, and thereby quantify QW structural disorder CITE Yoshita SIL/QW paper.

In addition to studying quantum well disorder, linear spectroscopy is useful for characterizing the energy profile of electron states in matter. For example, we can use linear spectroscopy to study exciton states and incoherent coupling in the asymmetric double quantum well (AQW). These systems are great testbeds for various quantum coupling phenomena CITE AQW Review, and understanding incoherent coupling between exciton states in asymmetric double quantum wells allows us to fulfill two important experimental goals: we obtain a better understanding of the exact absorption energies of the various exciton states. Ad-

ditionally, we can explore incoherent coupling mechanisms between exciton states in each of the wells. Particularly, we can explore the temperature and barrier width dependence of coupling between excitons in adjacent wells.

In this thesis, I present the development of a high-resolution micro-photoluminescence spectroscopy ( $\mu$ -PL) experiment to quantify QW disorder. Furthermore, I translate this spatial picture into a quantitative measurement of disorder on three different types of QW structures: a periodic ten-quantum well structure, a periodic four-quantum well structure, and an interfacial quantum dot ensemble. In addition to  $\mu$ -PL experiments, I present the development of Photoluminescence Excitation Spectroscopy (PLE) to study the incoherent coupling between exciton states in GaAs/InGaAs AQW structures. I will then use our PLE characterization of exciton states in AQWs to comment on and add to the relative paucity of information on thermal and barrier width mediation of coupling between exciton states in the stokes and anti-stokes directions.

This thesis is structured such that Chapter 2 is a theoretical introduction to the physical concepts necessary to understand our  $\mu$ -PL and PLE experiments. Chapter 3 will be a description of our experimental methods, while results of our experiments will be presented in Chapter 4. Chapter 5 will conclude this thesis with our experimental interpretations and a discussion of possible experimental directions for the future.

## **Chapter 2**

### **Theory and Background**

In this chapter, I will provide the theoretical background necessary to understand the work presented in this thesis. The first section will deal with the definition and importance of the bandgap of a material, the second will introduce the effects of confinement on electrons within semiconductors, leading to a discussion of experimental confinement within the semiconductor quantum well. The third section will introduce the concept of semiconductor quantum well disorder, and the fourth will motivate the study of semiconductor quantum well disorder with micro photoluminescence spectroscopy. Finally, I will discuss the optical properties of asymmetric double quantum wells and how to use photoluminescence excitation spectroscopy to investigate incoherent coupling between excitons in the asymmetric double quantum wells.

#### **2.1 The Semiconductor Quantum Well**

This section will broadly lay out band theory of electron states in solids. I will then discuss interband absorption by electrons in direct-gap semiconductors.

##### **2.1.1 Bandgap**

In order to understand how electrons behave in a crystalline solid, one must first understand how bound electrons act when arbitrarily many atoms are brought together in a lattice structure. Consider a collection of  $N$  atoms sufficiently far apart such that interactions

between atoms can be neglected. In this limit, electrons in an atom such as Hydrogen occupy discrete energy levels. For instance: suppose all  $N$  of our atoms are monatomic hydrogen atoms. In our system, an electron behaves according to the following Hamiltonian:

$$\hat{H} = -\frac{\hbar^2}{2m} \nabla^2 - \frac{e^2}{2\pi\epsilon_0 r}. \quad (2.1)$$

We can find the electron wavefunctions  $\psi(x)$  by solving the time independent Shrödinger equation,

$$\hat{H}\psi(x) = E_n\psi(x) \quad (2.2)$$

where  $E_n$  is the energy of the  $n^{th}$  energy level. This equation can be solved using the usual methods [11], but doing so here would be a diversion, so I'll just skip to the crucial points: evidently, the  $n = 2$  electron wavefunction (again neglecting interactions between atoms and ground state perturbations) is

$$\psi(x) = Y_l^m \frac{1}{\sqrt{2}} a_0^{-3/2} \left(1 - \frac{r}{2a_0}\right) \exp(-r/2a_0) \quad (2.3)$$

where  $a_0$  is the Bohr radius,  $Y_l^m$  is either the  $l = 0, m = 0$ , the  $l = 1, m = 1$ , or the  $l = 1, m = -1$  spherical harmonic. Note: each  $n = 2$  energy level in this system is  $N$ -fold degenerate, as there are  $N$  orbitals with the same energy. Considering just the  $n = 2$  states and neglecting perturbations, electrons in these states evidently all have energy

$$E_2 = \frac{-13.6 eV}{n^2} = \frac{-13.6 eV}{4}. \quad (2.4)$$

In the limit that many atoms are brought together such that interactions can no longer be neglected, two things happen: each  $N$ -fold degenerate electron energy level will split into  $N$  components, and these levels will become so close that they will smear into allowed and disallowed energy densities of state [13, 18, 11, 7, 8]. Roughly speaking, the occupied states are known as the “valence band” states, and the unoccupied states are known as the “conduction band states”. The energy difference between the valence band and conduction band is called the bandgap, and its importance will be illuminated momentarily.

These band states are simultaneous eigenstates of both the Hamiltonian and the crystal momentum [7, 8]. This means that bands can be easily depicted in k-space using dispersion curves. Dispersion curves map out allowed band energies in k-space, and their full functional shape is dependent on the types and arrangement of constituent atoms. Solids can be broadly organized into three categories based upon the k-space arrangement of their electron bands. In metals, the conduction band energies are below the highest energy valence band states and thus some conduction band states are occupied. In insulators, the bandgap is relatively large (about 10eV) [8]. By contrast in semiconductors, the bandgap is roughly 1eV and can therefore be optically accessed. Sometimes, as in the case of GaAs crystals, a local valance band minima and conduction band maxima occur for the same value of  $k$  in k-space. Semiconductors with this sort of bandstructure are known as direct-gap semiconductors. Around this value of  $k$ , electrons can absorb a photon with enough energy to undergo a direct transition from the valance band to the conduction band [13, 15]. This fact forms the basis of linear and nonlinear optical studies of semiconductor nanostructures [6], photonic devices, and certain types of theoretical quantum information processing schemes.

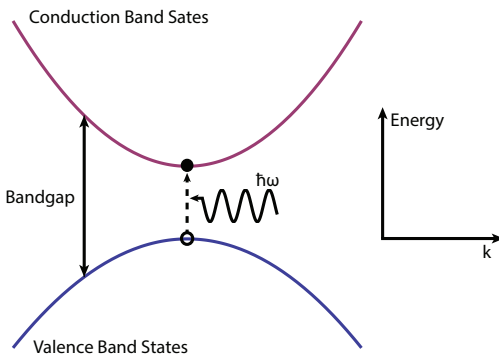


Figure 2.1: A typical dispersion curve minima for a direct-gap semiconductor. An optical transition is illustrated at  $k = 0$ , where an electron is absorbing a photon resulting in a transition from the conduction band to the valance band.

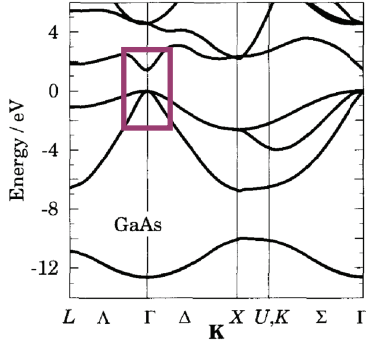


Figure 2.2: The band structure of GaAs, the allowed states are the thick horizontal curves, and the boxed region is the direct-gap region, in which electrons can make direct transitions across the bandgap. Note, the minima of this region look like the dispersion curve in figure 2.1 [7].

### 2.1.2 Confinement

It is well known that nanometer scale confinement of particles results in quantized energy states [11]. In the previous section, I briefly introduced the bandgap, and its important physical properties. In this section, I'll illustrate an interesting application of band theory: the semiconductor quantum well (QW). First, it is important to understand what we mean by confinement, and how quantized energy levels arise for confined particles. I will draw an analogy to a familiar physical situation, the particle confined within an infinite potential. I will then use this analogy to construct a physical picture for QWs, and then I will discuss the formation of excitons and a simple physical model of their behavior, sufficient for understanding the spectroscopy conducted in this thesis.

Perhaps the simplest problem in quantum mechanics is the of confinement of a particle in an infinite, one dimensional potential well. I will sketch a derivation of the wave function of a particle trapped in such a well, and use this derivation as the basis for exploring the physics of the QW exciton. We will begin by considering an arbitrary particle confined in a one dimensional infinite potential well. The potential that our arbitrary particle feels is:

$$V(x) = \begin{cases} 0 & 0 < x < L \\ \infty & |x| > 0 \end{cases}$$

where  $L$  is the length of the potential well. Graphically, the potential the particle feels looks like 2.1.2.

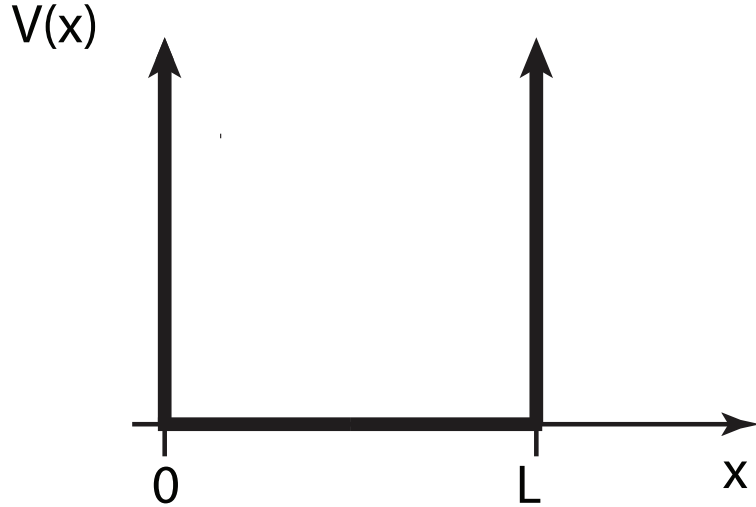


Figure 2.3: A graphical representation of the one-dimensional infinite potential well of width  $L$ .

Our task is to solve the time independent Schrödinger equation to show how quantized bound states arise for one-dimensional confinement. The time independent Schrödinger equation reads:

$$\hat{H}\psi(x) = E\psi(x) \quad (2.5)$$

where  $E$  is the energy of the particle, and  $\psi(x)$  is the particle's wavefunction. The particle will evidently be confined to the well, so our Hamiltonian inside the well is just

$$\hat{H} = -\frac{\hbar^2}{2m} \frac{\partial^2}{\partial x^2} \quad (2.6)$$

where  $m$  is the particle's mass, and  $E$  is the particle's total energy. The time independent Schrödinger equation now reads:

$$\frac{\partial^2}{\partial x^2}\psi(x) = -\alpha\psi(x) \quad (2.7)$$

where we define

$$\alpha = \frac{2mE}{\hbar^2}. \quad (2.8)$$

Now, eq. 2.7 looks like the familiar simple harmonic oscillator equation from classical mechanics. Because the wave function must be continuous at  $x = L$  and  $x = 0$ , i.e. it vanishes at those locations, and the potential is odd about the origin, solutions to eq. 2.7 have the form:

$$\psi(x) = A\sin(kx) \quad (2.9)$$

where  $k$  contains  $E$  and is determined by our boundary conditions. Now we want  $\psi(L)$  to vanish, but we can't have  $A = 0$ , because that is the trivial solution to eq. 2.7. Therefore, because we want  $\psi(L) = A\sin(kL) = 0$ , we must have  $ka = \pm n\pi$  where  $n \in \mathbb{N}$ . Now, we can absorb all of the negative combinations of  $kL$  into our normalization constant,  $A$ , and we have, then, that

$$k_n L = n\pi \quad (2.10)$$

where the subscript denotes the fact that we now have infinitely many, *discrete* solutions to eq. 2.5. Evidently

$$k_n = \frac{n\pi}{L} \quad (2.11)$$

and therefore

$$\psi(x) = A\sin\left(\frac{n\pi x}{L}\right). \quad (2.12)$$

Now, if we let  $k_n = \alpha$  and solve for  $E$ , we obtain

$$E = \frac{n^2\pi^2\hbar^2}{2mL^2}. \quad (2.13)$$

It will do us no good to normalize the wavefunctions we found, as their use for our purposes is minimal. The important part is that confinement in one dimension resulted in our particle occupying *discrete* energy levels whose energy depends on the size of the confinement potential.

Using layers of semiconductors, one can generate similar one-dimensional confinement effects for electrons. A simple way this can be done is by sandwiching a layer of low-bandgap semiconductor material in between two layers of higher bandgap materials [7]. One period of this structure is shown in figure 2.4. If the well material is a direct-gap semiconductor, then simple optical transitions (i.e. not mediated by phonons) across the bandgap can be made, as the transition illustrated in figure 2.1. Figure 2.5 is the band structure for GaAs, the chosen well material for the studies of growth disorder. Annotated on the figure is the direct-gap transition zone of interest. The potential well created by the semiconductor sandwich leads to quantization of electron states within the well layer [14, 7, 6]. We can access each of these states optically, making the QW a great testbed for exploring electron dynamics within a simple and well-known potential [6].

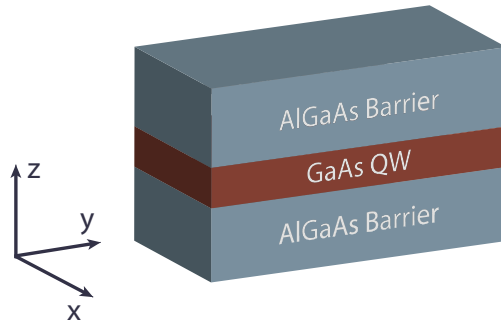


Figure 2.4: An example of the semiconductor quantum well. These layers can be repeated arbitrarily many times.

### 2.1.3 The Exciton

The simple picture presented above doesn't quite adequately represent the physics of an electron within a quantum well, however. After an excited electron moves from the valence band to the conduction band, it will leave behind a vacancy, or "hole", around its parent atom [14, 7]. The electron feels a *screened* Coulomb potential from this vacancy, as the vacancy is positively charged. I'll briefly sketch why this potential arises and then introduce the key concept of this section: the exciton. Imagine a number of electrons have been excited within the QW. Now, spatially, one will have a quasi-neutral distribution of electrons and holes in the well layer: an electron-hole plasma. I will assume that the holes are stationary relative to the electrons in the well, and that the excitation density is relatively low. These assumptions are *a priori* unphysical, but they immensely simplify the derivation of the electric potential QW electrons feel, and preserve the important physical results.

Let's explore the local behavior of an excited electron due to a single adjacent hole in the QW. Note that in this picture, electrons everywhere in the QW feel a Coulomb attraction to the hole, but the electrons adjacent to the hole screen its effects from charges far away. This phenomenon, known in plasma physics as Debye shielding [5] and in quantum mechanics as electron screening [11], modifies the pure Coulomb potential one would expect a single electron-hole pair to experience. We will assume that the electrons in the plasma obey a Maxwellian density distribution. Now, the local density of electrons around the hole is

$$n_e = n_0 \exp\left[\frac{e\phi}{kT}\right] \quad (2.14)$$

where  $n_0$  is the electron density far away,  $e$  is the electron charge,  $\phi$  is the local electromagnetic potential, and  $T$  is the electron temperature. A complete derivation for this electron number density in an arbitrary plasma can be found in CITE Chen. This is the local electron distribution, and we can assume  $e\phi \ll kT$  because the potential an electron feels due to one hole can be considered small relative to its thermal energy. Taylor expanding to first order,

we find that

$$n_e \approx n_0 \left[ \frac{e\phi}{kT} \right]. \quad (2.15)$$

Now, our local charge density is

$$\rho(r) = e \left[ \delta(r) - n_0 \left( \frac{e\phi}{kT} \right) \right] \quad (2.16)$$

where we've assumed that the hole has positive charge magnitude  $e$ , is infinitely small, and situated at the origin. The Poisson equation reads

$$\epsilon_0 \nabla^2 \phi(r) = -e \left[ \delta(r) + n_0 \left( \frac{e\phi}{kT} \right) \right]. \quad (2.17)$$

We can define a constant,

$$k^2 = \frac{n_0 e \phi}{\epsilon_0 k T} \quad (2.18)$$

and now the Poisson equation is

$$(\nabla^2 - k^2) \phi = -\frac{e \delta(r)}{\epsilon_0}. \quad (2.19)$$

This is known as the screened Poisson equation, and its solution is

$$\phi(r) = -\frac{e}{4\pi\epsilon_0 r} e^{-kr}. \quad (2.20)$$

Now,  $\phi(r)$ , functionally, the correct result (albeit with a different  $k$ ) had we proceeded under the Thomas-Fermi approximation, assuming only that the potential is weak and varies smoothly and slowly over a distance around the hole equivalent to  $\frac{1}{k_f}$ . This turns out to be a very good approximation for the local potential an electron feels relatively close to a hole CITE Patterson. The single-particle hamiltonian for an electron in the QW is now:

$$\hat{H} = -\frac{\hbar^2}{2m} \frac{\partial^2}{\partial x^2} - \frac{e}{4\pi\epsilon_0 r} e^{-k_0 r} \quad (2.21)$$

where  $k_0^2 = \frac{n_0 e \phi}{k T_f}$  is the “corrected”  $k$  for the same potential derived under the Thomas-Fermi approximation [16].

Note that if the potential electrons feel was exactly Coulombic in nature, then any bound state between an electron and a hole would be hydrogenic [11]. This potential, however, is *not* exactly Coulombic in nature, so the bound states between the electrons and holes can't be described by hydrogenic wavefunctions. Nevertheless, bound states between an excited electron and an adjacent hole do exist, and when an electron and hole occupy these states, they form a quasiparticle called an "exciton", and they can be treated as a single particle with an effective mass [13, 7].

The subtleties of the wave function are treated in [13], exploring their exact functional form and corresponding density of exciton states in the QW will not be of use to us here. Only energy levels of the QW exciton are discretized by its confinement, those of excitons created in the bulk are not. A final important note: in both my derivation and those proceeding under the Thomas-Fermi approximation, the hole is assumed to be a *stationary* point particle. This is emphatically *not* true, but the physics doesn't change that much if we assume both charge carriers are mobile. Excitons can still be treated as a single particle even removing this assumption. Figure 2.5 depicts a simple physical picture for excitons: the electron and hole excited energy levels can be thought of as the ground state of a particle trapped in a finite potential.

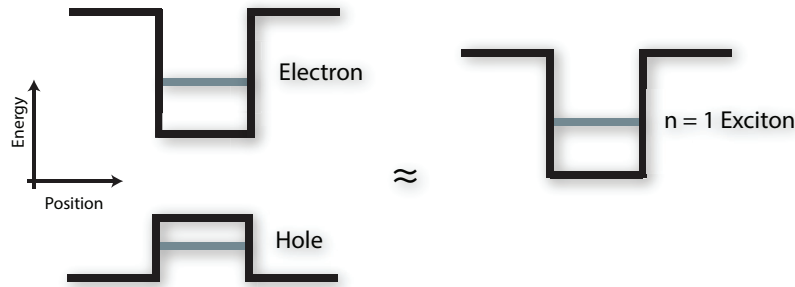


Figure 2.5: A simple model for the behavior of an exciton in a quantum well, suitable for the work completed herein.

## 2.2 Quantum Well Disorder

When an exciton is optically created, in a direct gap semiconductor such as GaAs, the charge carriers can recombine from either exciton “ground” state ( $n = 1$ ), or “excited” states ( $n > 1$ ) and emit a photon at the exciton binding energy [9]. Since I am only interested in linear, long-timescale exciton physics, we can treat QW excitons as an approximately two-level system, only looking at ground state recombination. The emission energies for QW excitons will be dependent on well depth, a function of the barrier composition, and well width. Control of QW layer thickness has improved immensely, as QW structures can be made to precise specifications with modern molecular beam epitaxial growth methods [7]. However, imperfections of layer width on the order of a crystal monolayer occur unavoidably at the interface between the well and barrier materials during the QW manufacturing process [21] paper (find better). In figure 2.6, an AFM picture of imperfections of a GaAs surface are shown. These defects, known as structural disorder, slightly change the width of the well layer and thus subtly modulate exciton emission energies, an illustration of which is shown in figure 2.7. By analogy to eq. 2.11, excitons localized in slightly thinner than average sections of the QW will emit at slightly higher energies than average. Conversely, excitons localized in thicker than average sections of the QW will emit at slightly lower energies than average. Thus, structural disorder is the main contribution to inhomogeneous broadening in the QW coherent optical response [4].

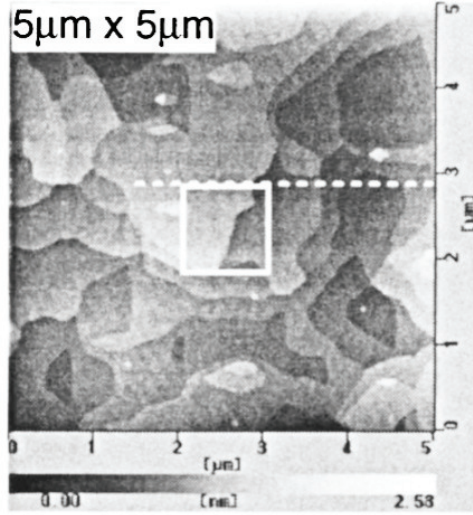


Figure 2.6: An STM picture of the GaAs growth front, stopped mid-growth, of a 110 oriented sample. The shown defect size is roughly representative of disorder in modern GaAs samples grown by molecular beam epitaxy. However, defect size and shape is highly sample dependent, so disorder varies widely from one QW structure to the next. Note, the disorder terraces are on the order of 100nm across. Adapted from [21].

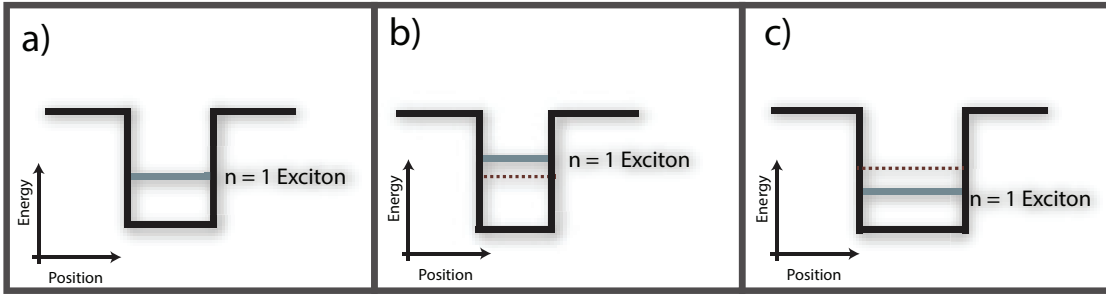


Figure 2.7: In a), the energy of a ground state exciton located in a portion of the QW of average thickness, the blue line in b) depicts the ground state energy of an exciton located in a slightly thinner than average portion of the QW, and in c), the blue line depicts the ground state energy of an exciton located in a slightly thicker than average portion of the QW. In both b) and c), the average exciton ground state energy is depicted by the maroon dashed line.

### **2.3      Exciton Coupling in Asymmetric Double Quantum Wells**

Quantum coupling between excitons occurs when multiple quantum wells get close enough so that the exciton wavefunction can tunnel slightly into adjacent wells [11, 7]. In order to study quantum coupling between states in adjacent QWs, however, it is not simply enough to grow multiple quantum well layers fairly close to one another. Evidently, if each of the wells is of identical thickness, then QW PL from one well will be spectrally indistinguishable from another. Indeed, it is necessary to grow wells of varying thickness when studying coupling in multiple quantum wells [12].

Asymmetric multiple quantum well (AQW) samples are a convenient system in which to study exciton coupling between wells. Incoherent coupling between exciton states, through temperature mediated CITE Borri T, dipole-dipole interactions [19], or other incoherent processes can be quantified. Photoluminescence Excitation spectroscopy (PLE), a linear technique, can provide information on the energies and locations of various exciton states in AQWs. Coupling between wells is of interest because an improved understanding of the various processes that govern carrier transfer in nanostructures can help improve the efficiency and quality of nanostructure devices like photodiodes and transistors. Additionally, an increased understanding of exciton coupling processes is of fundamental research interest.

### **2.4      Microphotoluminescence Spectroscopy**

Because local QW thickness determines exciton emission energy, a spatial picture of disorder is possible through spectral imaging. By using a continuous wave (CW) excitation source to create a population of QW excitons and monitoring the emission energy as a function of sample position, one can extract the local QW width [4]. With sufficiently high resolution, obtaining a map of emission energies for a representative portion of a QW sample is possible. In order to obtain a map of emission energies, one must monitor the photoluminescence (PL) energies as a function of position. In a PL experiment, light of

sufficiently high energy is shown on a sample, exciting a large number of charge carriers to the conduction band. During this process, electrons fall back into holes in the valance band, emitting a photon equivalent to the lost energy [7]. If a QW exciton recombines, it will emit a photon equivalent the energy difference between the valance band and one of the quantized exciton states. If we regard the exciton as a two level system, by exciting QW excitons near-resonantly, the energy of the emitted photon will be equivalent to the energy difference between the valance band and the exciton ground state.

In order to obtain an image of PL, we must collect the signal carefully. More precisely, if we are to obtain a spatial picture of QW disorder, we must collect and spectrally resolve a PL image. The PL will be emitted from the exciton population over a  $4\pi$  solid angle, so we must place the QW directly at the focus of our imaging system in order to form a clear PL image. Furthermore, since the scale of the disorder is on the order of 100nm [21], we must have comparable resolution for the PL image. Measuring a PL image is fairly easy, one must place the QW at the focus of a pair of lenses in a confocal optical geometry. Figure 2.8 is a diagram of this setup, and the magnification of the PL image is set by the ratio of the lens focal lengths. Namely,

$$M = \frac{f_1}{f_2} \quad (2.22)$$

where  $f_2$  and  $f_1$  are the focal lengths of the short focal length lens and the long focal length lens respectively, and  $M$  is the image magnification factor. A PL experiment with sub-micron resolution which is capable of spectrally resolving a PL image is known as a “microphotoluminescence spectroscopy” experiment, or  $\mu$ PL.

As simple as the PL image collection is, it is difficult to obtain the requisite image resolution because the PL is around 750-800nm wavelength, but as I've asserted above, the islands can be smaller than this. What this means is that if we were able to image at the Abbe diffraction limit of our optical geometry, we still wouldn't have the resolution necessary

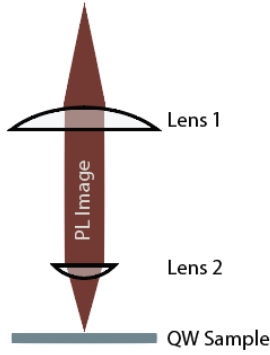


Figure 2.8: A representation of a confocal optical geometry used to collect the PL from the QW sample. The PL image is being collected from a small region of the QW sample, magnified, and then collimated by the two lenses.

to resolve adjacent disorder sites. The Abbe diffraction limit is

$$d = \frac{\lambda}{2nNA} \quad (2.23)$$

where  $\lambda$  is the wavelength of the PL image,  $n$  is the index of refraction in the intermediate space between the sample and lens 2 (the imaging lens) in figure 2.8, and  $NA$  is the numerical aperture of lens 2. Note that  $NA = f/D$  where  $f$  is the focal length of the imaging lens and  $D$  is its diameter. In our case,  $d \approx 500\text{nm}$  for  $\lambda \approx 780\text{nm}$ ,  $n = 1$  in vacuum, and we pick  $NA = .83$ , as that was the NA of the lens in our experimental setup.

In order to get around this limit, we either need to resort to exotic microscopic techniques, or we can employ a fairly simple trick. It has been shown that by increasing the index of refraction ( $n$ ) with a solid immersion lens (SIL), the Abbe diffraction limit can be substantially reduced [22] paper, and broad SIL paper. In order to do this, one simply places a hemisphere of sufficiently high  $n$  material between the sample and the imaging lens. Figure 2.9 is a diagrammatic representation of this improvement. Note, I'll use SIL and hemisphere interchangeably from here on out, though they aren't necessarily interchangeable, as "SIL"

refers to a truncated sphere of some degree.

In my experimental setup, I used a Zinc Selenide (ZnSe) SIL, for which  $n = 2.4$  at  $\lambda = 780nm$ . This improvement decreases the diffraction limit from  $d \approx 500nm$  to  $d \approx 185nm$ , roughly sufficient resolution for our purposes. I'll expand on the precise setup in the next chapter, but the experiment will be very similar to what I've just described.

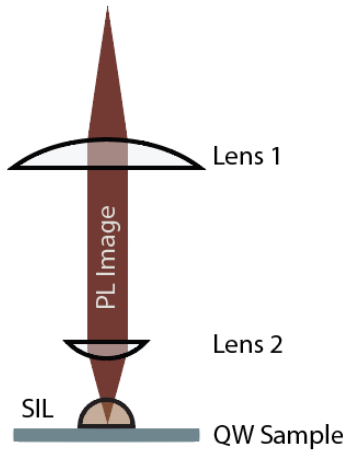


Figure 2.9: A representation of the principle of our specific  $\mu$ PL experiment. The PL image leaves the SIL normal to the hemispheric surface, so it just increases  $n$  and lowers the diffraction limit.

## 2.5 Photoluminescence Excitation Spectroscopy

I employ photoluminescence excitation (PLE) to study exciton coupling in AQW systems. PLE is a simpler method than  $\mu$ PL, as only the relative PL intensity is monitored. Generally, one looks at PL amplitude at a specific wavelength as the excitation wavelength is scanned across a wide range of wavelengths. By monitoring the PL as a function of excitation wavelength, one obtains a measure of absorption by the sample [8]. By extending this technique slightly, I can quantify the coupling between excitons in AQW samples. In order to do this, I scan the excitation wavelength of our light source, and take a PL spec-

trum (not just a single intensity value) for each different excitation wavelength. That way, the emission from both wells can be monitored as a function of excitation wavelength, and coupling between wells can be quantified: as the excitation wavelength scans over an exciton resonance in one well, the PL signal from the other well can be monitored to see if that resonant excitation increases emission.

## **Chapter 3**

### **Experimental Methods**

In this chapter I will describe the experiments I conducted for this thesis. The first section will deal cover the configuration and customization of the continuous wave (CW) Titanium Sapphire laser I used as an excitation source for conducting both PLE and  $\mu$ PL experiments. Section two will cover the design and construction of the in-cryostat optic mount for the  $\mu$ PL experiment as well as the optical configuration for data collection. Section three will illustrate the data collection procedure used in  $\mu$ PL experiments, as well as the function and implementation of LabView code I wrote for hardware control and data acquisition. In section four, I will lay out the optical design of our PLE experiments and in section five, I will discuss the experimental data collection process and signal optimization routines.

#### **3.1 The Light Source**

The PLE and  $\mu$ PL experiments required a CW laser light source with a few properties: the laser must be a stable and fairly high-power light source with narrow line-width. For  $\mu$ PL, it was important that we have a fairly Gaussian and symmetric beam so we could obtain the desired spot-size and resolution at the sample. Additionally, conducting PLE scans required that we have the ability to computer control the laser wavelength over a fairly broad range of wavelengths, roughly a spectral region from  $\lambda = 780\text{nm}$  to  $\lambda = 850\text{nm}$ . The laser we chose for this task was a Schwartz Electro Optics Titan-CW Titanium Sapphire

(Ti:Sapph) laser. Its specifications were fairly close to our needs, as its specified operating power is 500mW with a tunable range from roughly 700-820nm [20].

The laser cavity can be configured for either CW or pulsed operation. In CW operation a 532nm pump beam, 5W of power, enters the cavity through a series of steering mirrors. After entering, the pump passes through a lens to focus the pump on the Ti:Sapph crystal. After the gain medium, the remaining pump light passes through the end mirror and terminates at the back of the laser enclosure. The laser configuration is shown in figure 3.1.

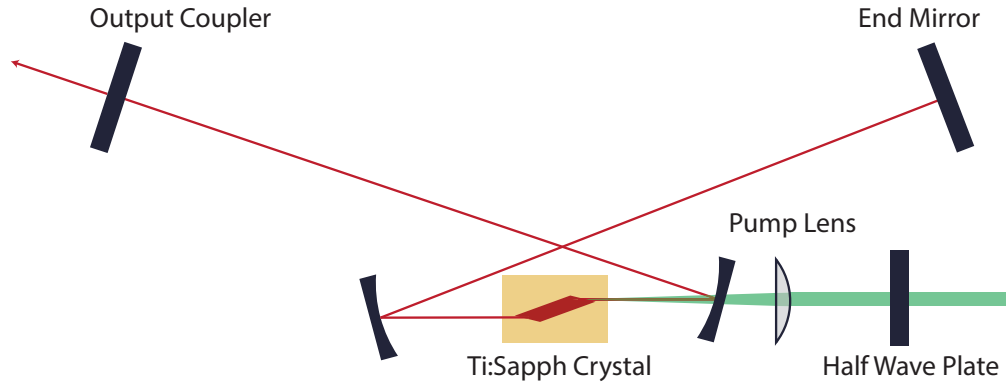


Figure 3.1: A depiction of the modified mount: the actuator arm fits into a sleeve attached by a pivot to the rotating filter mount. A spring attached to both the rotating mount and aluminum block holds the sleeve to the actuator and ensures smooth rotation in either direction.

Though the Ti:Sapph laser nearly met our specifications, it required two modifications to be operable in our experiments. First, we needed to add a computer controlled actuator to rotate the birefringent tuner in order to allow for increased tunability and repeatability relative to a manually actuated micrometer. We modified the rotation mount for the birefringent filter (BRF) to accommodate a Newport TRB25 linear actuator. The linear actuator pushed a spring-loaded arm to rotate the BRF to a specified angle and select our desired wavelength. Figure 3.2 depicts the modified BRF mount with the actuator attached.

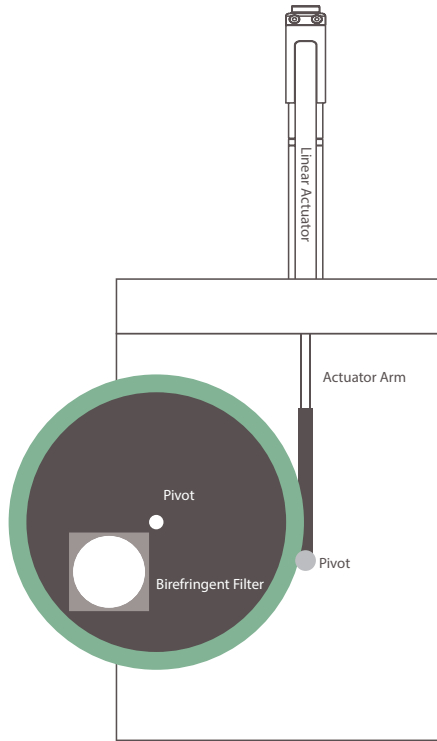


Figure 3.2: A depiction of the modified mount: the actuator arm fits into a sleeve attached by a pivot to the rotating filter mount. A spring attached to both the rotating mount and aluminum block holds the sleeve to the actuator and ensures smooth rotation in either direction.

### 3.2 Optical Components and Optical Path Configuration for $\mu$ PL Experiments

#### 3.2.1 Manufacturing the SIL

In order to obtain the resolution necessary to image disorder, the experiment employed a solid immersion lens (SIL) at the surface of the sample to increase the index of refraction at the imaging plane. I chose ZnSe as the SIL material, as its index of refraction at 780nm is  $n=2.53$  [1]. However, ZnSe SILs are not commercially available, so I resorted to manu-

facturing SILs from a stock ZnSe window. The window measured 2.54cm diameter by 1cm thickness, and our goal was to manufacture SILs of roughly 3mm in radius. To begin, we used a core drill, diameter 6.35mm, to cut out a cylindrical chunk of ZnSe. I then centered and glued the cylindrical stock material to a brass dowel, 2mm in radius. After the ZnSe was glued to the rod, the SIL shaping began. I put the brass dowel in a power drill used 200 grit sandpaper to shape the ZnSe cylinder roughly into a hemisphere.

When the SIL was in the roughly correct shape, we lapped and polished the hemispherical surface until the SIL was the correct size. Additionally, since the experiment required optical quality surfaces, this was a careful and fairly lengthy process. I made the polishing lapps by machining a 2.54cm diameter copper rod to roughly 2cm in diameter with a 1.8cm wide by 1cm deep cavity. Then, I melted lead solder into the cavity, let it harden, and machined the face of the copper and solder until they were flush and machine-smooth. Then, I pressed a cleaned, 6.35mm diameter ball bearing halfway into the solder. Figure 3.3 depicts what a finished lapp looked like before it was used to grind and polish the SIL.

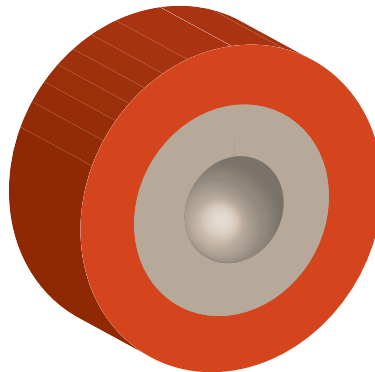


Figure 3.3: A depiction of the lapp. The orange casing is copper while the grey lining is lead solder. The cavity left by the ball bearing was smooth enough to polish the relatively soft ZnSe hemispheres to an optical quality finish.

After the lapp was made, we mounted the dowel with the SIL attached to a glass-working lathe. As the lathe rotated, we placed the lapp with a mixture of glass polishing

solution of various grit and mineral oil onto the SIL and held it in place with a sharpened wire. The wire and Lapp were set off-center relative to the SIL so the friction of the rotating SIL would randomly move the lapp so as to evenly polish the surface of the hemisphere. A depiction of this setup is in figure 3.4. We iterated polishing runs, changing the lapp each time we stepped down in grit size. After the polishing process finished, the SIL was removed from the dowel and the flat surface was polished with a colloidal silicon mixture. When the SIL was finished, we had a hemispherical (to within 1%) ZnSe SIL.

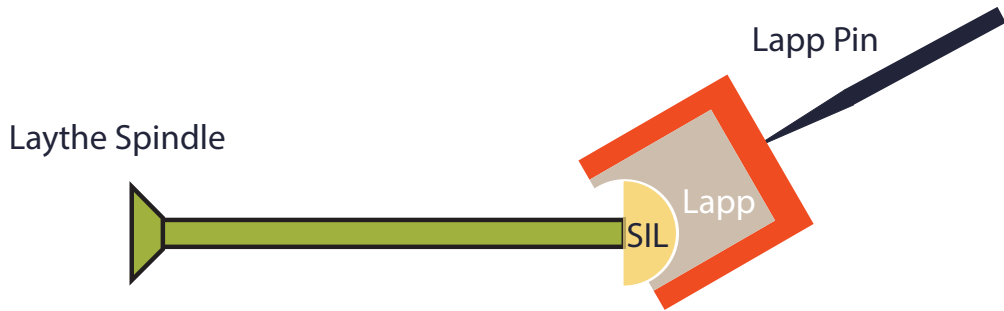


Figure 3.4: A depiction of the polishing setup in the lathe. The off-center placement of the lapp and lapp pin allowed the lapp to rotate and move slightly to randomize the SIL polishing.

### 3.2.2 Manufacturing the Cryostat Optics Mount

In order to achieve the desired imaging resolution, our chosen optical geometry (refer to 2.4) required a high-NA lens as the imaging lens. We therefore chose an Edmund Optics 0.83*NA*, 9mm effective focal length aspheric lens. Together with our ZnSe SIL, this gave us an Abbe diffraction limit of  $d = 185.05\text{nm}$  for PL centered around  $\lambda = 780\text{nm}$ . This diffraction limit is less than our goal of  $d = 200\text{nm}$ . As our experiment required cooling to cryogenic temperatures, we had to build a mechanically and thermally stable optics platform to hold the lenses and QW sample together in the correct configuration. Therefore, working with our machinists, I designed an optics mount to hold the in-cryostat optical components

which are seen in Figure 3.5. The optics mount stands vertically in our Cryo-Con 8CN bath cryostat. Therefore, since the excitation laser enters the cryostat vertically, we designed the optics mount to be held to a mirror which filled the entire optics mount and was positioned at a 45 degree angle so as to direct the laser to the sample and capture the total PL image. The mirror was ground by taking a stock Thor Labs 2.54cm diameter mirror, protecting the silvered face with weak glass tape, cutting the mirror to 3mm thick, and securing the mirror to an aluminum rod of 15mm diameter (the same diameter as the inside of the optic mount). The end of the rod was bevelled at 45 degrees, and the mirror and rod combination was spun by hand on the side of a glass cutting saw blade. This process ensured that, when the glass was cut flush with the edge of the rod, the mirror was the correct elliptical shape and diameter to fit in the optics mount. The mirror was then secured to a roughly .5mm thick sheet of indium which was epoxied to the mirror mount.

### **3.2.3 Experimental Optical Path Configuration**

Our aim was to characterize disorder over an area roughly  $200\mu\text{m}$  in diameter. In order to do so, we needed the laser spotsize to be  $200\mu\text{m}$  in diameter or larger. Additionally, to obtain clear images, the excitation spot needed to be monotonic, symmetric, and preferably Gaussian in shape. To this end, I characterized the laser spot size and found it to be  $1.6 \pm .1\text{mm}$  FWHM diameter, roughly Gaussian and symmetric to within 20%. In order to obtain the requisite beam diameter at the sample, it was necessary to resize the beam going into the cryostat. In order to do so, we used a succession of four lenses to resize the beam. The first two lenses, one of focal length 60mm and the other of focal length 25.4mm, shrunk our beam from 1.6mm to 0.68mm. The second lens in the second pair of lenses was the in-cryostat asphere, and in combination with the lens outside the cryostat, focal length 30mm, resized our beam to  $203\mu\text{m}$  in diameter. After the beam hit the sample, the PL signal travelled through the asphere and out of the cryostat. We placed a 90% reflective non-polarizing beamsplitter (NPBS) outside the cryostat to pick off the PL signal.

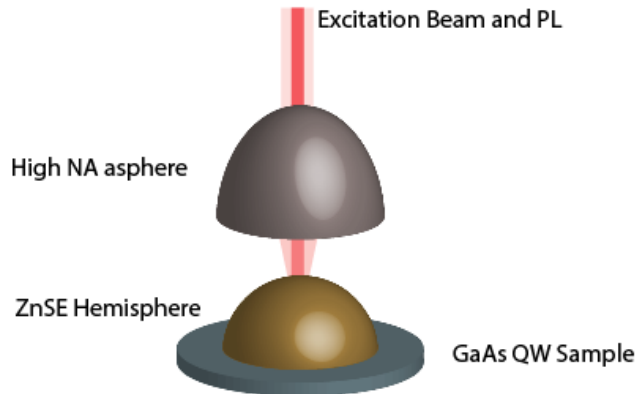


Figure 3.5: A representation of the optics inside the cryostat. The optics were held in place relative to each other by a gold-plated copper mounting tube, containing the lenses. This mounting tube was affixed to a mirror which directed the excitation beam into the cryostat optics and eventually the sample.

The beamsplitter sent the PL signal through an achromatic, 20cm focal length lens, and a polarizer to filter out the laser. Finally, the signal focused onto the slit of a Horiba iHR550 imaging spectrometer. The 20cm lens was 50.4cm in diameter and mounted to a linear translation stage. Its function was to focus the PL spot on the spectrometer slit and translate the image across the spectrometer slit, as in Figure 3.7. The PL image was roughly 9mm in radius at the lens, so since the lens was relatively large compared to the image, spherical image aberrations during image translation were negligible.

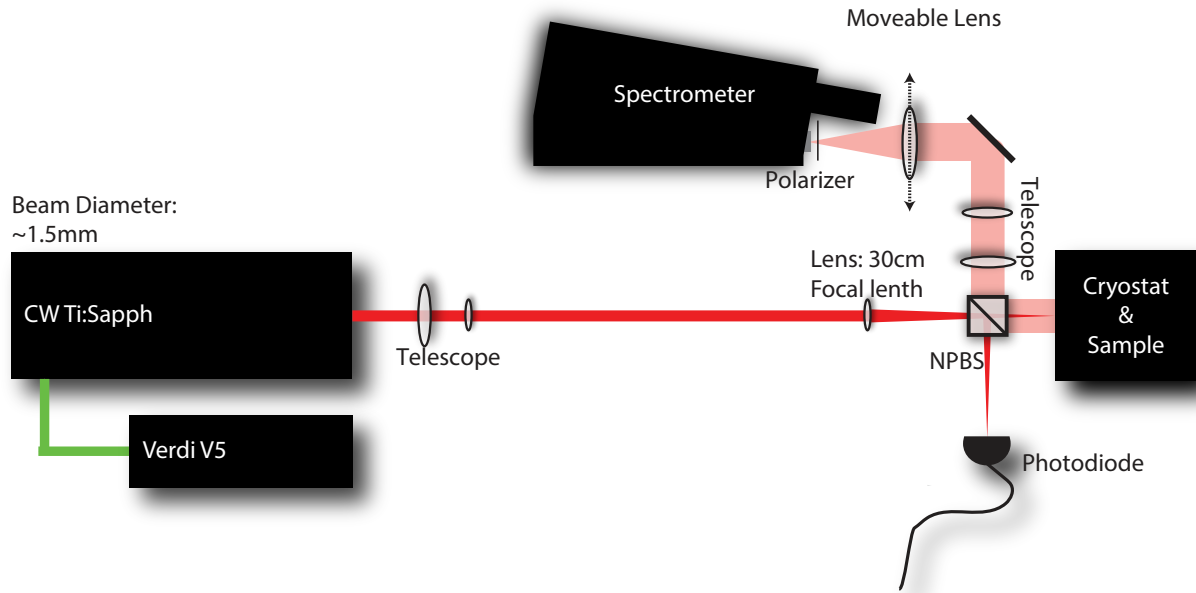


Figure 3.6: A diagram of the experimental components. The second telescope was an optional feature, its use doubled the system magnification. The light pink beam is the PL signal, while the red beam is the excitation laser.

We monitored the laser power with a photodiode, using the light that was dumped out of the experiment by the NPBS. Additionally, between the NPBS and the moveable lens, we had the option to add a telescope to improve the magnification of the system further. The use of the telescope depended on the intensity of the signal. If the signal was vanishingly small, the telescope made it nearly unreadable. Therefore, in cases where less signal reached the spectrometer, the telescope became impractical.

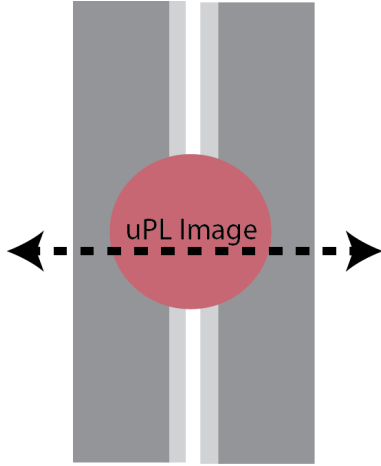


Figure 3.7: A depiction of the PL spot on the spectrometer slit. The spot translates across the slit as we move the lens on the translation stage, allowing us to take vertical slices of the image as it translates across the slit.

### 3.3 $\mu$ PL Data Collection

#### 3.3.1 Optical Alignment Considerations

When the optical components were roughly in the configuration seen in Figure 3.6, we cooled the sample to  $10 \pm 1\text{K}$  and adjusted the laser power to  $100 \pm 1\text{mW}$  so that the laser power at the sample was roughly  $1\text{mW}$  at the sample (because the NPBS dumped 90% of the power we fed into it). We identified the PL signal using a polarization filter, as it was the only signal left after the filter was rotated such that its polarization was orthogonal to that of the beam reflected from the sample. We set the position of the 30cm lens by maximizing the size of the PL image while monitoring it with an IR viewer as we adjusted the position of the lens. Then, we experimentally adjusted the focus of the moveable lens to maximize the spatial differences seen in PL amplitude on the CCD. Finally, we put the polarizer just in front of the spectrometer slit and rotated it to cut out as much laser scatter from the signal as possible.

### 3.3.2 Data Collection Process

The data collection process was fairly simple. The spectrometer CCD recorded an intensity image 1024x2048 pixels large. The vertical pixel dimension corresponded to vertical spatial dimension on the sample, while the horizontal pixel dimension corresponded to PL emission wavelength and both axes could be calibrated such that we could read peak emission wavelength as a function of vertical sample position. Each image we recorded was effectively a vertical slice of the larger two dimensional PL image. If we step-translated the PL image across the spectrometer slit and took an image at each lens position, we could recover both PL intensity and PL energy as a function of position. This is exactly the information required to reconstruct a spatial map of QW disorder.

The computer control of the experiment involved five pieces of hardware: two linear actuators, a photodiode, the spectrometer and the imaging CCD. The photodiode was read by the analog-to-digital converter of a Stanford SRS 810 lock-in amplifier using General Purpose Interface Bus (GPIB) protocol. The lens translation stage was actuated by a Newport TRB12 linear actuator, and it was controlled (along with the laser wavelength adjustment) by a Newport ESP300 motion controller interfaced through GPIB. Both the Horiba spectrometer and CCD interfaced over USB. The manufacturers of each of the above devices wrote LabView interface code which I incorporated into my overall experimental control code. The experimental control and data acquisition process proceeded according to the flowchart in Figure 3.8. The collected images and photodiode readings were handled and analyzed with MATLAB code that I wrote, included in Appendix A.

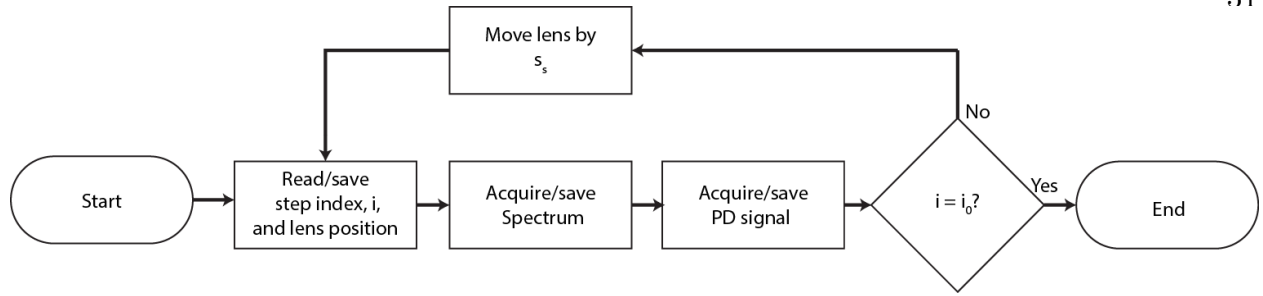


Figure 3.8: A flowchart depicting the LabView code processing sequence. Each set of  $\mu$ PL data was acquired using this process, where  $s_s$  was the lens step size and  $i_0$  was the number of data collection steps to be run.

### 3.4 Optical Components and Optical Path Configuration for PLE Experiments

#### 3.4.1 Optical Path Configuration and Alignment

Because we didn't need to image the PL from the QW sample in PLE experiments, the optical configuration simplified immensely. The laser first went into an NPBS where about 10% of its power was directed at a photodiode to monitor the laser power during acquisition. From there, the laser travelled to a 7.5cm focusing lens. The lens focused the laser onto our InGaAs/GaAs QW samples, which were rotated at 45 degrees with respect to the laser path to minimize reflected laser light arriving at the spectrometer. The sample was kept in a Janis FIND OUT MODEL helium vapor flow cryostat with tunable temperature control. The PL signal was collected by the same 7.5cm focusing lens, and then sent through a polarizing beam splitter whose polarization was orthogonal to the laser's. Following the beamsplitter, the PL signal was sent to the same achromatic 20cm focal length lens used as the moveable lens in the  $\mu$ PL experiments. After the lens, the PL signal passed through another polarizer rotated orthogonally to the laser polarization to minimize the laser light entering the spectrometer. The signal then passed into the spectrometer where it was collected as a spectral trace instead of a spectral image. We took data over an area of the CCD which measured 100x2048 pixels.

We then integrated over the vertical pixels and recorded spectra which were intensity vs. horizontal pixel number which we calibrated to wavelength. Figure 3.9 is a diagram of the experimental setup. Note, we modified the laser slightly by replacing the output coupler with one coated to work at wavelengths longer than 800nm so we could sweep the laser wavelength out to 850 or 860nm during PLE runs. Only negligible changes to the beamsize and output power resulted from this change.

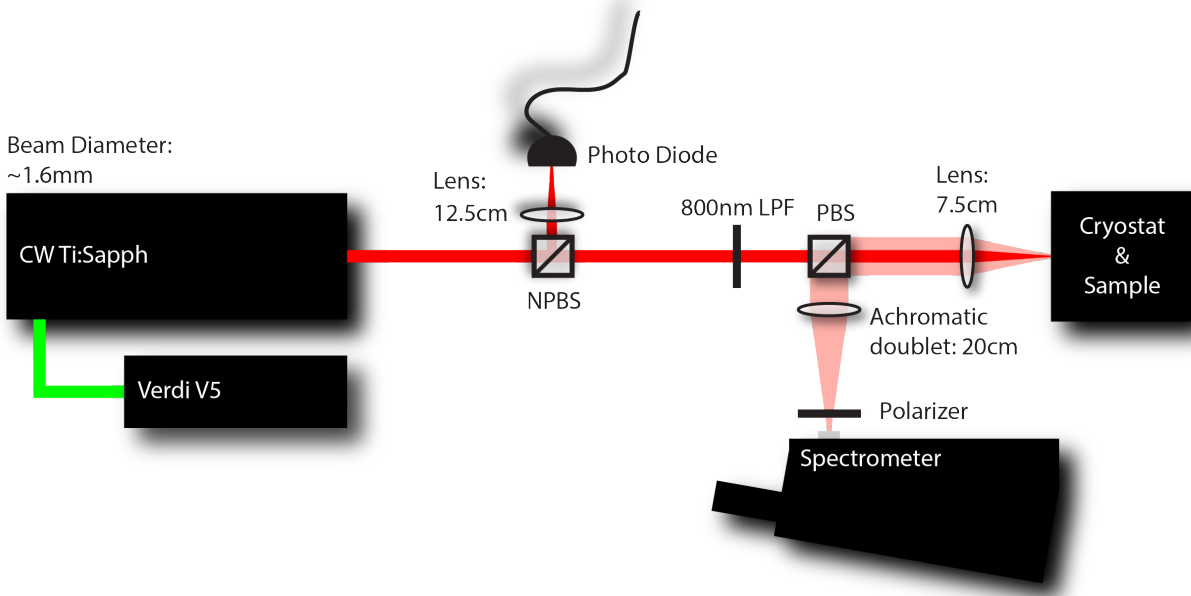


Figure 3.9: A diagrammatic representation of the PLE experiment. The red beam is the excitation laser while the pink beam is the PL signal. We used a long pass filter (LPF) to cut out any light with wavelength lower than 800nm, as we suspected some of the pump scatter (green) was making it to the sample, reducing our ability to control the excitation wavelength.

### 3.4.2 Data Collection for Photoluminescence Excitation Spectroscopy

The PLE data runs were fairly similar to those used for taking  $\mu$ PL data. The computer interfaced with the spectrometer, the photodiode, and the laser wavelength actuation in the

same way. During the data collection process, we monitored spectral response as a function of wavelength, recorded these spectra, and then changed the excitation wavelength of the laser. The sets of PLE spectra, BRF actuator position, and PD signal were collected and processed using MATLAB and Igor. Figure 3.10 is a flowchart representing the LabView code I wrote for the data collection process.

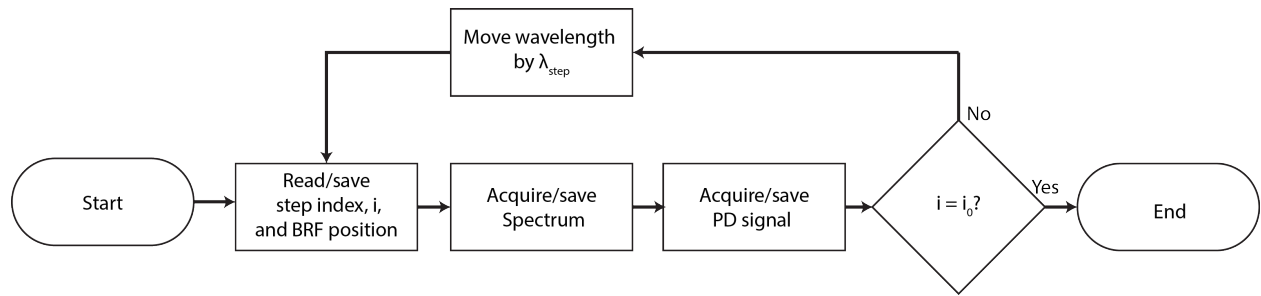


Figure 3.10: A flowchart depicting the LabView code processing sequence for the PLE experiments. Each set of PLE data was acquired using this process, where  $\lambda_{step}$  was the wavelength step size and  $i_0$  was the number of data collection steps to be run.

## Chapter 4

### Disorder in Quantum Well Structures

#### 4.1 $\mu$ PL Results and Analysis for Multiple Quantum Well Samples

##### 4.1.1 Disorder in a Ten Quantum Well Structure

As a proof-of-concept test for our  $\mu$ PL experiment, we decided to measure the structural disorder in a ten-period 10nm GaAs QW with 10nm AlGaAs barriers in between wells. Note: for the following discussion, the ten-period QW and the four-period QW samples will be referred to as the 10QW and 4QW samples respectively. We expected to see a large PL signal from this sample. Therefore, it was our goal to measure a PL image of the 10QW sample, with our laser exciting near-resonantly. Our excitation wavelength was 773nm, while our detection center wavelength was 812nm, and the PL signal peaked around 808nm. Figure 4.1 shows a single raw image corresponding to a vertical slice of the total PL image.

From the raw spectrometer images, we found the wavelength corresponding to the maximum PL amplitude at each vertical CCD maximum and read that pixel's PL wavelength and amplitude information. We then compiled that information into either a PL amplitude or PL energy as a function of vertical sample position surface. Effectively, at each lens position, we took a vertical slice of the raw image and stacked that information along the lens translation direction to obtain a 2D image. Figure 4.2 shows a representative vertical image slice from the images taken on the 10QW sample. From this, we found a total PL image from the 10QW sample, seen in Figure ???. The larger structure in the PL image correspond to artifacts on the surface of the QW sample: despite our best efforts, surface

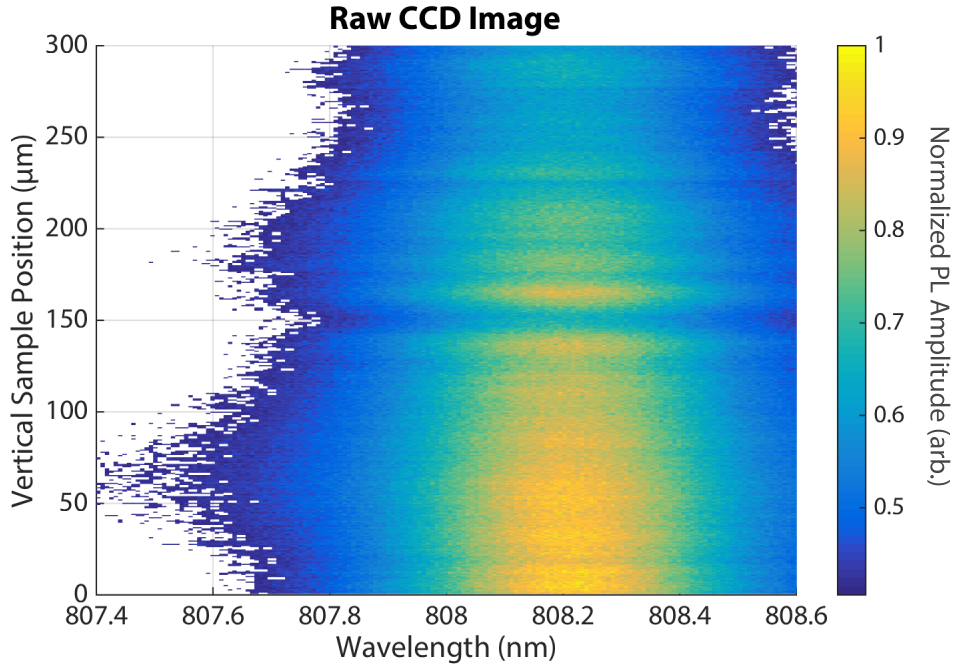


Figure 4.1: A raw CCD image corresponding to one vertical slice of the PL image. In order to calculate the PL emission wavelength as a function of sample location, we found the maximum PL amplitude as a function of vertical sample position for each vertical slice.

imperfections and dust were present on the sample during data runs. However, the fact that we are actually able to produce a PL image reconstruction which shows the imperfections as defined reductions in PL signal indicates that the sample surface was in focus, and we are near the maximum image definition we can expect for the disorder map.

From this image, we can estimate the resolution limit for the PL image alone. Doing so, we calculated that the resolution limit for our imaging system was limited by the repeatability of the lens position,  $0.5\mu\text{m}$ , which corresponds to 225nm at the sample surface. We were limited in the vertical direction by the pixel size, which was  $13.6\mu\text{m}$ . Because our magnification factor was 22.22x, our vertical resolution was no better than 612nm on the sample. This was not our goal of 185nm; however, one can ameliorate this issue by inserting a telescope, with 2x magnification, between the NPBS and the achromatic doublet. An un-

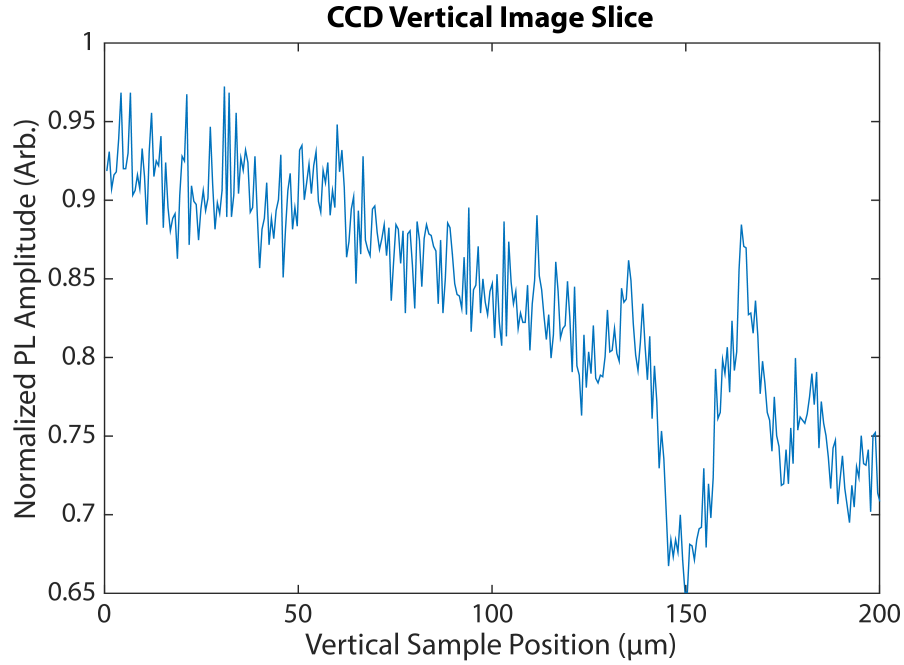


Figure 4.2: A vertical 10QW PL amplitude slice from a CCD raw image. Effectively, these slices were stacked together along the lens translation axis to recover the second sample location axis and build a 3D surface of either PL amplitude or PL energy.

fortunate side effect of increased resolution, however, was decreased signal strength. It was therefore necessary to increase CCD integration time or increase PL emission by increasing excitation power, but as we were exciting the sample with an already relatively high power of 1mW, increasing the resolution necessitated increasing integration time. For the 4QW sample, we took data with the telescope in place, but for the 10QW sample, a resolution of 225.0x612.0nm was the best we achieved.

Though our resolution was less than optimal, we were still able to calculate an energy deviation map for the 10QW sample. To do this, we found the emission energy corresponding to the maximum PL amplitude at each vertical pixel. After doing this, we stacked each of these points (for which we had an energy vs. vertical sample position vector) along the horizontal image axis at each lens position. Once done, we then calculated the average PL

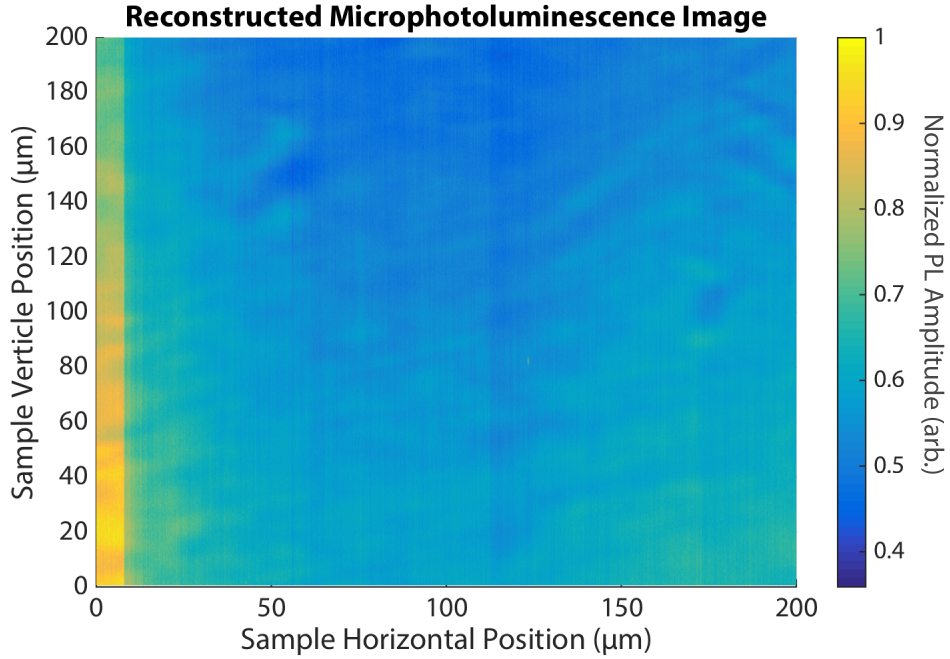


Figure 4.3: A reconstructed PL image of 10QW sample surface. The small features in the image correspond to striations and dust on the surface of the sample. The excitation spot's maximum intensity occurred near the bottom of the image, corresponding to the PL amplitude maximum.

energy for the entire PL image. Then, we found the local energy deviation from the average PL energy by subtracting the average PL energy from the local PL energy. Simply:

$$\delta E_{i,j} = E_{i,j} - E_{avg} \quad (4.1)$$

where  $E_{avg}$  is the average emission energy for the whole PL picture, and  $i, j$  index horizontal and vertical sample position respectively. Following this, we obtain our  $\mu$ PL map. However, this map is too noisy to see structure, as CCD intensity fluctuations of roughly 10 counts or 1% of the total signal will affect which PL peak amplitude, and thus the peak energy at a given sample location location. Therefore, we must take our  $\mu$ PL energy deviation map and Gaussian smooth the energy deviation values by two to five pixels FWHM depending on the sample. Doing so, we obtain the energy deviation map seen in Figure 4.4.

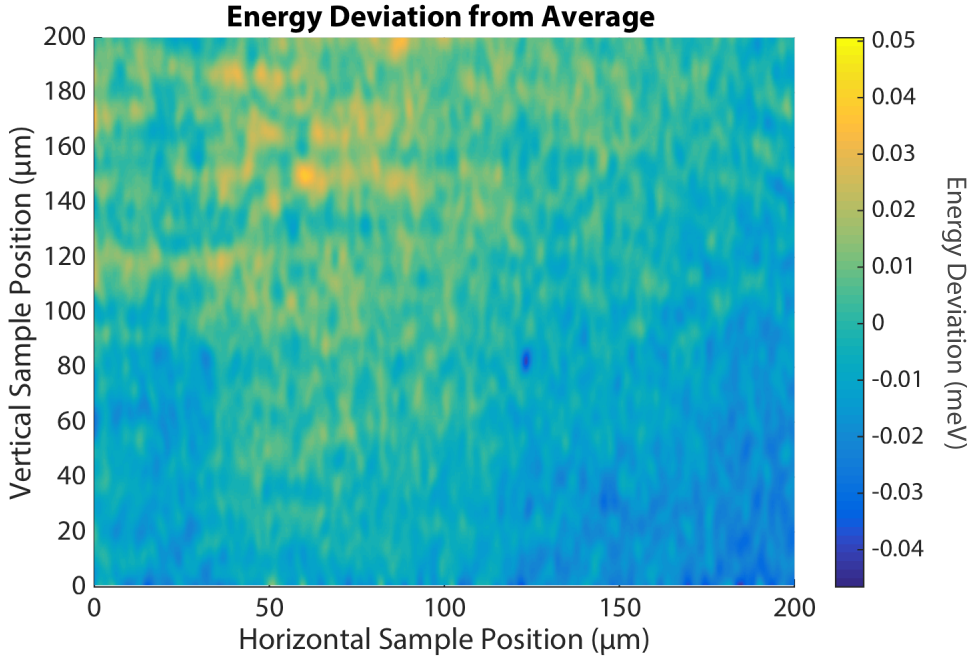


Figure 4.4: A  $\mu$ PL energy deviation image for the 10QW sample. Note the energy deviation was found to be 0.1meV, peak to peak, at maximum.

We expected energy deviations as a result of QW width fluctuations to behave according to the following equation:

$$\delta E = \frac{\hbar^2 \pi^2}{2\mu_{HH}} \left( \frac{1}{(L^* \pm a)^2} - \frac{1}{L^{*2}} \right) \quad (4.2)$$

where  $\delta E$  is the PL energy deviation due to a well width fluctuation of  $\pm a$ ,  $\mu_{HH}$  is the heavy-hole reduced mass, and  $L^* = L + 2\delta$  is the effective well width accounting for electron wave-function penetration of 15Å into the AlGaAs barrier, and  $\mu_{HH} = 0.055m_e$  is the reduced exciton mass [10, 17]. We saw energy deviations of about ??meVpp, which was five times less than expected. This discrepancy was due for the most part to signal averaging within the 10QW sample PL image: the relatively weak PL signal from spots in the wells which deviated from average width was most likely from the first few wells, and not all 10QWs. Additionally, since we looked only at the maximum amplitude PL signal from each point in the sample, due to the random distribution of disorder, the maximum PL energies

at each PL image location would tend to be close to the average PL energy for the whole sample, as the signal at each location was presumably an average over the QW emission from each well at each imaging location. In other words: the way we took our PL image meant that any disorder deviations we saw would be due to the additive effects of disorder over multiple wells, meaning that disorder fluctuations were smaller than expected in the one QW limit. Using Equation 4.2, we expect energy deviations of roughly 0.5meV for disorder variations of one crystal monolayer. Anything less than this corresponds to no measured well width variations whatsoever.

#### 4.1.2 Disorder in a Four Quantum Well Structure

Because the 10QW PL energy deviations due disorder was fairly small, we decided to take  $\mu$ PL data on a four-period 10nm GaAs QW with 10nm AlGaAs barriers. As 4QW sample had fewer wells, but each was identical in width to the 10QW sample, we expected to see larger disorder energy deviations because there would be fewer wells over which the signal would be averaged. Additionally, we inserted a telescope into the PL imaging path, increasing our on-sample resolution. In the horizontal direction, the resolution limit was no longer set by the lens translation. Rather, since we were able to magnify our image by 2x, the horizontal resolution was diffraction limited to  $192.9 \pm 0.3$  nm, as our PL wavelength peaked around 807.8nm, with a FWHM of 0.6nm. The vertical resolution was increased by a factor of two from 612.0nm to 306.0nm. Therefore, for the 4QW sample, our on-sample resolution was theoretically  $192.9 \times 306.0$  nm. This is close to our goal of a completely diffraction-limited system, but we weren't quite able to achieve that in the vertical imaging direction. However, due to high image noise, we applied a Gaussian blur to our energy maps to recover their underlying structure. Therefore, though our PL image had a resolution of  $192.9 \times 306.0$ , our energy 4QW map was limited to a resolution of 252x400nm. Figure 4.5 is a reconstructed PL image collected from the 4QW sample, while figure 4.6 is the image deviation map corresponding to the PL image.

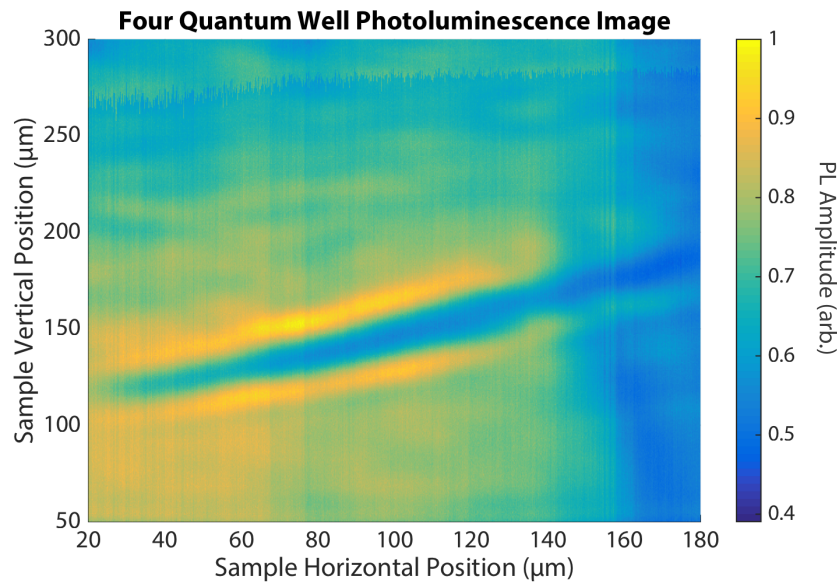


Figure 4.5: A reconstructed image of the PL amplitude of the 4QW sample.

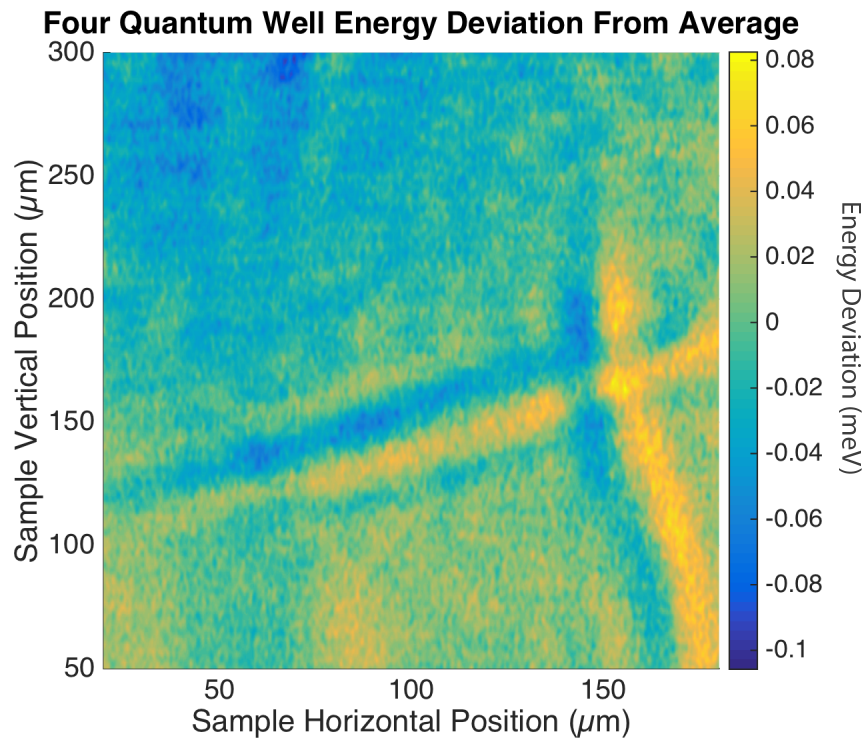


Figure 4.6: An energy deviation map for the 4QW sample.

With the periodic 4QW structure, we were running into the same problems we had with

the 10QW sample: due to spectral averaging over multiple quantum wells, we saw energy deviations corresponding to well width variations of less than a monolayer. Though the energy deviations from disorder for each single quantum well were presumably larger than those we saw, we weren't able to resolve the disorder variations due to a single quantum well.

#### 4.1.3 Disorder in an Interfacial Quantum Dot Structure

Our final disorder measurement was taken on an interfacial quantum dot (IQD) sample. Due to high signal averaging for the MQW samples, we weren't able to see the energy deviations we theoretically should have. Subsequently, we took  $\mu$ PL data on a 5-period, varying well and barrier thickness GaAs/AlGaAs quantum well. Due to the growth process of the IQD sample, large well width variations translated into three-dimensional exciton confinement [15, 8], rather than just the one QW confinement dimension. Additionally, due to the larger well-width variations, disorder influences on PL energy were much larger. This is clear in Figure ???. Though the sample was a five-period structure, the increased structural disorder allowed us to see larger variations in PL energy relative to the 10QW and 4QW samples, as seen in 4.7. Additionally, due to the smaller well width for some of the IQD wells relative to the other two QW samples, our original light source was slightly unreliable at the shorter wavelengths necessary to probe IQD disorder: as we tuned the Ti:Sapph laser below 750nm, it would occasionally enter multi-mode operation. When this occurred, the laser would operate at diminished and unstable power. We therefore used a green laser, centered at 532.15nm to excite the IQD sample.

From these measurements, we were able to calculate a maximum PL energy deviation of 0.74meV, peak to peak. This value was much larger than the value found for both the 10QW and 4QW structures. Therefore, we were able to measure well width variations greater than one monolayer in the IQD sample. Though there was still spectral averaging due to the fact that the IQD sample was five wells thick, this larger variation was due to larger width

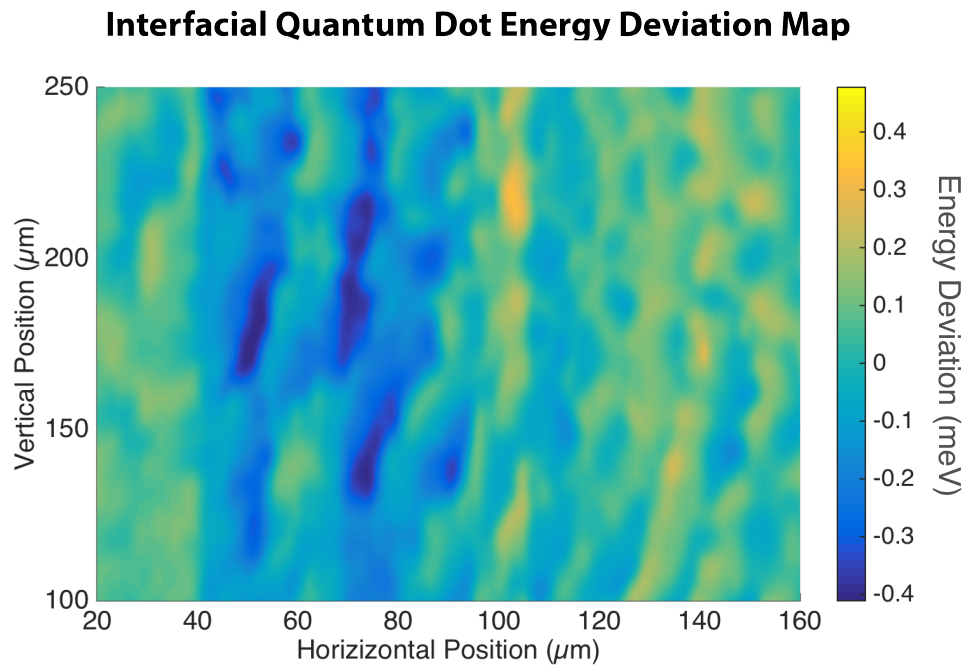


Figure 4.7: An energy deviation map for the IQD sample. The energy deviations in the IQD sample are much larger than those measured in the 4QW and 10QW samples, even though the IQD structure is periodic and suffers from similar spectral averaging the other two samples do.

fluctuations in the IQD wells and the diversity of well widths present in the IQD sample by design.

## 4.2 PLE Results and Analysis

For our asymmetric double quantum well samples, we had InGaAs wells of 9nm and 10nm with a GaAs barrier between them. We had three samples of varying barrier thickness,  $b$ , with  $b = 5, 10$ , or  $30\text{nm}$ . For each sample, we excited with our CW laser, and collected PL from the sample. We then stepped our laser excitation wavelength and monitored the PL spectra as a function of CW excitation wavelength. We found in each case that there was incoherent Stokes- and anti-Stokes coupling of excitons between wells. Figure 4.8 shows a close-up of the coupling peaks.

Traditionally, PLE is done by monitoring emission intensity at a single wavelength [3], but with our experiment, we are able to measure a full spectrum at each excitation wavelength. This ability means that our PLE spectra are more rich, as they provide simultaneous information of both narrow and wide well emission. Taking vertical slices along the emission peaks from the narrow and wide wells, we obtain information on exciton population by monitoring the emission amplitudes. We can then plot PLE emission amplitude as a function of excitation wavelength and monitor the strength of the Stokes- and anti-Stokes cross peaks as well as other peaks in emission corresponding to exciton ground and excited state emission. Figure 4.9 is an assembly of vertical PLE slices for three PLE spectra recorded at 10K. Note: as the barrier width decreases, the strength of the Stokes- and anti-Stokes peaks increases.

Figure 4.9 shows increased coupling between wells as barrier width decreases: both the red dashed trace peak around  $1.46\text{eV}$  and the blue trace peak around  $1.47\text{eV}$  increase as barrier width decreases. We measure, then, what we expect qualitatively: as AQWs get closer together, the incoherent coupling between excitons in each well increases. However, we were initially surprised that we measured coupling in the anti-Stokes direction. Intuitively, one would expect that an exciton excited in the wider well, since it exists at a slightly lower

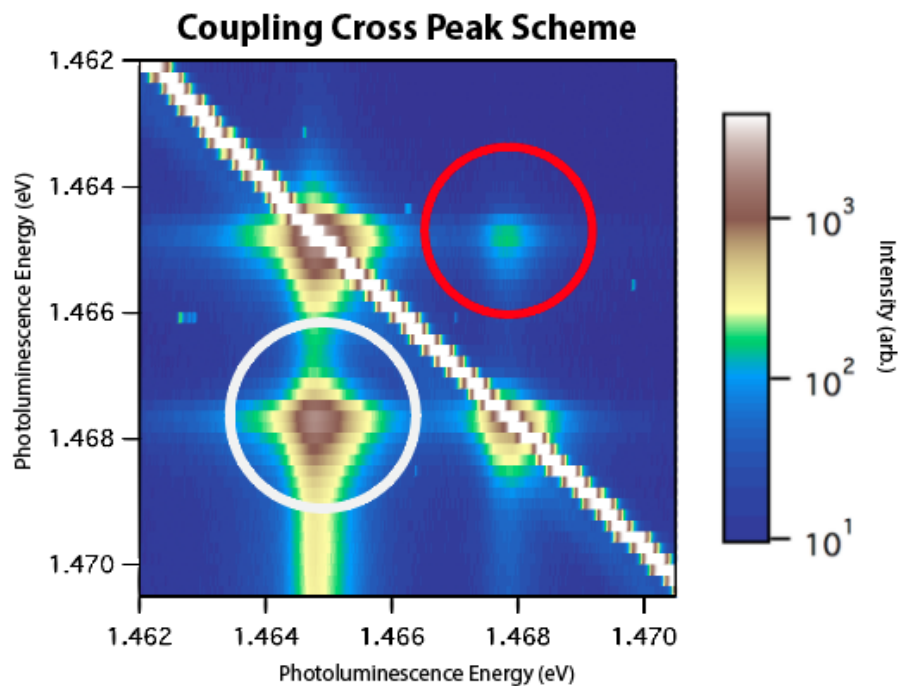


Figure 4.8: An example set of PLE data taken on AQW samples. The grey circle corresponds to a coupling peak between wells in the Stokes direction: the narrow well absorbs the laser excitation, while the wide wells emit a portion of the absorbed energy. The red circle corresponds to a coupling peak in the anti-Stokes direction: the wide well absorbs and the narrow well emits a portion of the excitation energy. The diagonal white trace is the laser scatter.

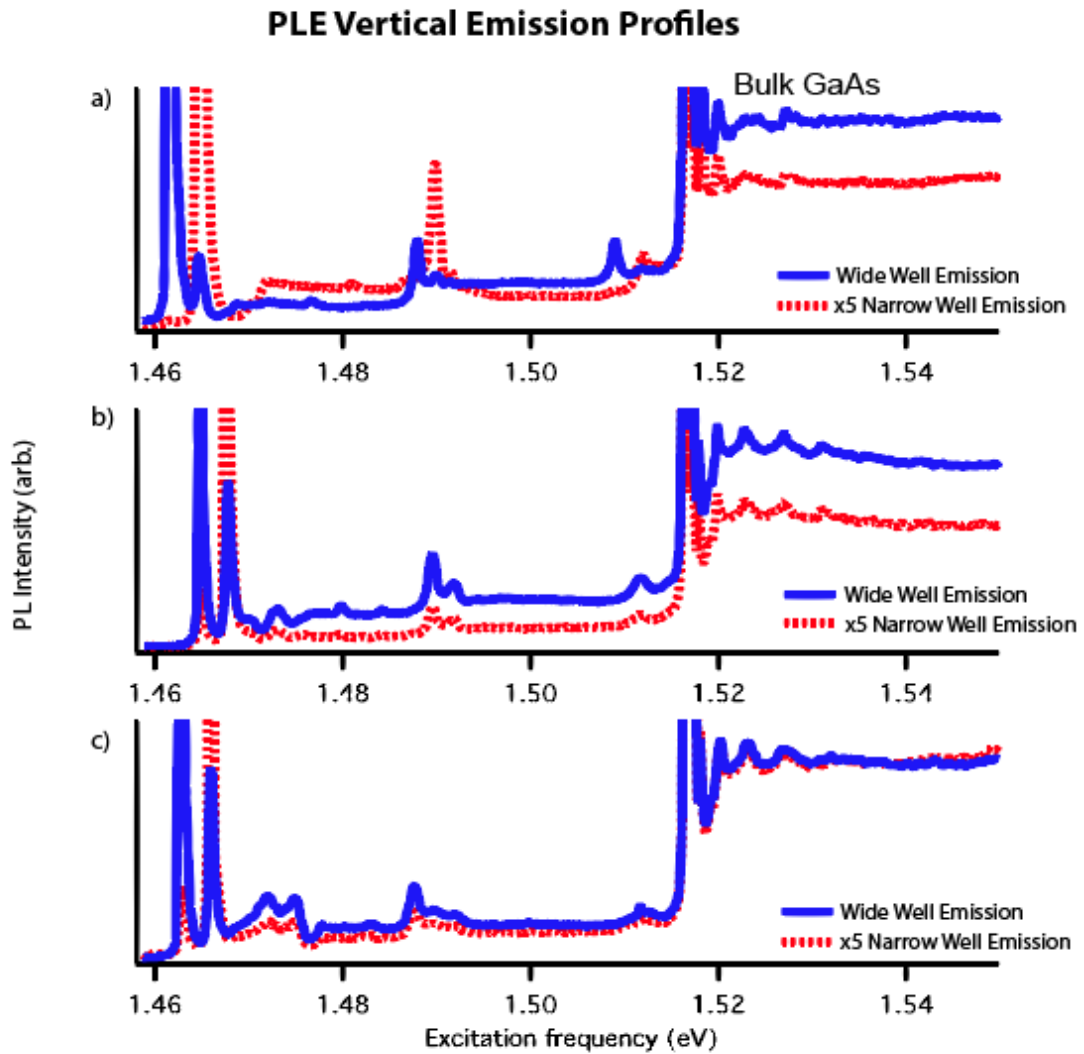


Figure 4.9: A set of three PLE vertical profiles taken at the wavelength of peak emission intensity for a) the 30nm, b) the 10nm, and c) the 5nm barrier width AQW. Note: the narrow well emission intensity was much lower than the wide well emission intensity, and was scaled up for graphical comparison.

energy, would not be able to emit from a state in the narrower well. We suspected, therefore, that coupling in the anti-Stokes direction would be a temperature mediated process. As a result, we took PLE data on all three barrier sizes and monitored the cross-peak intensity as a function of temperature. Figure 4.10 shows that the coupling between wells seems to be a temperature mediated process. Others have seen this temperature-dependence of coupling in the anti-Stokes direction, [3] but have failed to provide a model that accounts for the intensity of the coupling peaks as a function of temperature and of barrier width.

### Coupling Temperature Dependance

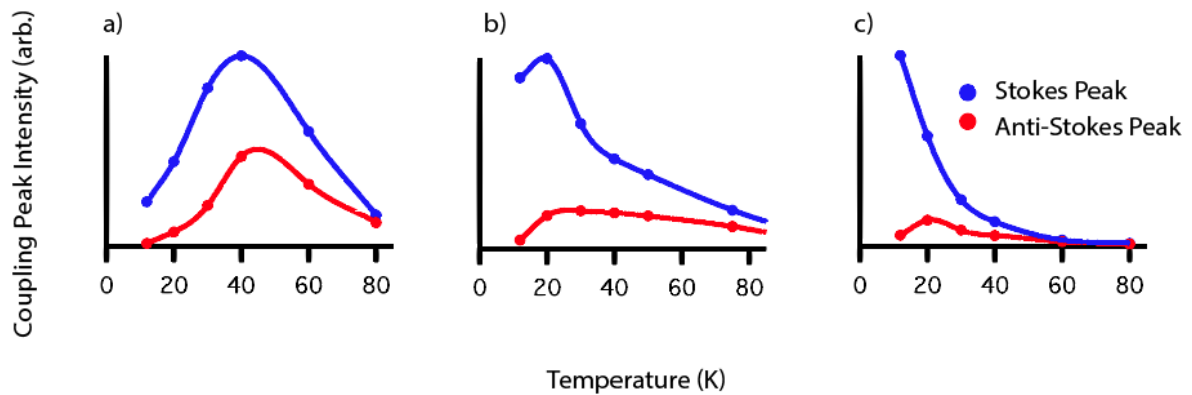


Figure 4.10: Temperature dependance for the PLE coupling peaks for barrier width of a) 30nm, b) 10nm, and c) 5nm. The intensity of coupling between wells seems to peak at some low temperature, and then decrease as sample temperature increases.

## Chapter 5

### Conclusion and Future Work

#### 5.1 Conclusions from Linear Spectroscopic Experiments

In this thesis I've presented the development of a way to obtain a spatial and spectral picture of semiconductor quantum well disorder. I have shown, furthermore, that we can obtain the desired quantification of disorder for a variety of QW systems. However, due to spectral averaging, this method is unable to distinguish the disorder contributions from individual wells in MQW samples. This was to be expected, however, as over more than two quantum wells, the disorder effects on PL energies smear out and have the effect of broadening PL line-widths.

In more disordered systems, like IQDs,  $\mu$ PL provides a unique way to measure spatial disorder. When the effects of spectral imaging can be minimized, such as in our IQD samples or in single QW samples, this method can provide adequate spatial resolution to resolve the effects of disorder on PL emission energies at the small disorder size scales.

Taken as a whole: I showed, with the data taken on the 4QW system, that with a sufficiently high magnification, it is possible to achieve the spatial resolution necessary to image structural disorder. Furthermore, with the data taken on the IQD system, I showed that our method has the ability to provide a spectrally resolved picture of PL emission. Therefore, with the correct samples (highly disordered QWs or presumably single QWs), we can use this method successfully to quantify structural disorder in semiconductor nanostructures.

I showed that incoherent coupling between AQW excitons can be studied in detail with

our enhanced PLE measurements. The richness of the data we retrieve using a spectrometer allows us study coupling in both the Stokes and anti-Stokes directions simultaneously. When employed to study the temperature dependance and barrier width dependance of incoherent coupling between QW excitons, we showed that our enhanced PLE technique is capable of producing a wealth of data about coupling strength and PL line-shapes that otherwise would not be possible.

## 5.2 Future Work

A natural next step for the  $\mu$ PL experiments we conducted would be to study single quantum well samples to see if we can, as in the case with IQDs, extract adequate spatial and spectral data from the PL signal to quantify the disorder of a single well, as that result is more easily generalizable than the IQD  $\mu$ PL result. Additionally, it would be useful to combine  $\mu$ PL data taken, on MQW or other QW samples, with two-dimensional Fourier transform spectroscopy taken on the same samples to see how localization and disorder affect the nonlinear optical response of QW excitons.

Our PLE studies of AQW systems proved useful in locating exciton states and quantifying incoherent coupling between exciton states in the adjacent wells. We could further our understanding of incoherent coupling by developing a better understanding for thermal mediation of coupling that adequately treats both temperature and barrier width dependance, as authors have independently addressed those questions in the past [3, 2, 19].

## References

- [1] Refractive index of ZnSe (Zinc selenide) - Connolly.
- [2] M. Batsch, T. Meier, P. Thomas, M. Lindberg, S. W. Koch, and J. Shah. Dipole-dipole coupling of excitons in double quantum wells. Physical Review B, 48(16):11817, 1993.
- [3] P. Borri, M. Guriolo, M. Colocci, A. Patanè, M. Grassi Alessi, M. Capizzi, and F. Martelli. Carrier transfer between ingaas/gaas quantum wells separated by thick barriers. physica status solidi (a), 164(1):227–230, 1997.
- [4] Alan D. Bristow, Tianhao Zhang, Mark E. Siemens, Steven T. Cundiff, and R. P. Mirin. Separating Homogeneous and Inhomogeneous Line Widths of Heavy- and Light-Hole Excitons in Weakly Disordered Semiconductor Quantum Wells. The Journal of Physical Chemistry B, 115(18):5365–5371, May 2011.
- [5] Francis F. Chen and Francis F. Chen. Introduction to plasma physics and controlled fusion. Plenum Press, New York, 2nd ed edition, 1984.
- [6] Steven T. Cundiff. Optical two-dimensional Fourier transform spectroscopy of semiconductor nanostructures [Invited]. JOSA B, 29(2):A69–A81, 2012.
- [7] John H. Davies. The physics of low-dimensional semiconductors: An introduction. Cambridge University Press, 1998.
- [8] Mark Fox. Optical properties of solids. Oxford master series in condensed matter physics. Oxford University Press, Oxford ; New York, 2001.
- [9] M. A. Gilleo, P. T. Bailey, and D. E. Hill. Free-Carrier and Exciton Recombination Radiation in GaAs. Physical Review, 174(3):898, 1968.
- [10] Yuri D. Glinka, Zheng Sun, Mikhail Erementchouk, Michael N. Leuenberger, Alan D. Bristow, Steven T. Cundiff, Allan S. Bracker, and Xiaoqin Li. Coherent coupling between exciton resonances governed by the disorder potential. Physical Review B, 88(7), August 2013.
- [11] David Griffiths. Introduction to Quantum Mechanics. Pearson, 2 edition, 2005.

- [12] J. Hegarty, L. Goldner, and M. D. Sturge. Localized and delocalized two-dimensional excitons in GaAs-AlGaAs multiple-quantum-well structures. *Physical Review B*, 30(12):7346, 1984.
- [13] Giuseppe Iadonisi, Giovanni Cantele, and Maria Luisa Chiofalo. *Introduction to Solid State Physics and Crystalline Nanostructures*. Springer, 2014.
- [14] David AB Miller. Optical physics of quantum wells. *Quantum Dynamics of Simple Systems*,” ed. G.-L. Oppo, SM Barnett, E. Riis, and M. Wilkinson (Institute of Physics, London, 1996), pages 239–266, 1996.
- [15] Galan Moody. *Confinement Effects on the Electronic and Optical Properties of Semiconductor Quantum Dots Revealed with Two-Dimensional Coherent Spectroscopy*. PhD thesis, University of Colorado, Boulder, 2013.
- [16] James Patterson and Bernard Bailey. *Solid-State Physics*. Springer Berlin Heidelberg, Berlin, Heidelberg, 2010.
- [17] Paulo V. Santos, M. Willatzen, M. Cardona, and A. Cantarero. Tight-binding calculation of spin splittings in semiconductor superlattices. *Physical Review B*, 51(8):5121–5129, February 1995.
- [18] D. B. Sirdeshmukh, L. Sirdeshmukh, K. G. Subhadra, and C. S. Sunandana. *Electrical, Electronic and Magnetic Properties of Solids*, volume 207 of *Springer Series in Materials Science*. Springer International Publishing, Cham, 2014.
- [19] A. Tomita, J. Shah, and R. S. Knox. Efficient exciton energy transfer between widely separated quantum wells at low temperatures. *Physical Review B*, 53(16):10793, 1996.
- [20] unk. Titan-CW Ti:sapphire laser Operation Manual. Technical report, Schwartz Electro-optics.
- [21] Masahiro Yoshita, Naoki Kondo, Hiroyuki Sakaki, Motoyoshi Baba, and Hidefumi Akiyama. Large terrace formation and modulated electronic states in (110) GaAs quantum wells. *Physical Review B*, 63(7), January 2001.
- [22] Masahiro Yoshita, Takeaki Sasaki, Motoyoshi Baba, and Hidefumi Akiyama. Application of solid immersion lens to high-spatial resolution photoluminescence imaging of GaAs quantum wells at low temperatures. *Applied Physics Letters*, 73(5):635, 1998.